PORE COMPRESSIBILITY OF RESERVOIR SANDSTONES FROM INTEGRATED LABORATORY EXPERIMENTS

by

Anvar Guliyev

A thesis submitted to the Faculty and the Board of Trustees of the Colorado School of Mines in partial fulfillment of the requirements for the degree of Master of Science (Petroleum Engineering).

Golden, Colorado

Date _____

Signed: _____
Anvar Guliyev

Signed: _____
Dr. Manika Prasad
Professor of Petroleum Engineering
Thesis Advisor

Golden, Colorado

Date _____

Signed: _____
Dr. Erdal Ozkan
Professor and Head
Department of Petroleum Engineering

ABSTRACT

Understanding the pore structure and the compressibility changes with formation pressure is crucial for determining reservoir properties. Knowledge of these parameters is essential in optimization of hydrocarbon production. Fluid removal from a reservoir increases the effective stress causing reduction of porosity and permeability, and changes pore compressibility. While pore compressibility, and pore compressibility and porosity relationship have been studied extensively, there is a lack of research done on pore compressibility from Nuclear Magnetic Resonance (NMR) relaxation. The method consists of determining the pore compressibility by looking at the change in porosity values as a function of confining pressure. This method of pore compressibility determination will provide us with static measurement, which is closer to rock properties at reservoir conditions. Using the NMR tool, we can determine the pore compressibility of individual pore structures in the reservoir.

In this study, I investigate pore size distributions and pore compressibilities for Hibernia and Berea sandstone samples. The Hibernia samples exhibit homogeneous mineralogy and wide range of porosities and permeabilities. I present pore compressibility values, determined from NMR and spectral induced polarization (SIP) pore size distribution, as well as pore compressibilities, calculated from helium porosimetry (CMS-300), and ultrasonic velocity measurements. SIP and CMS-300 data were used to validate the NMR pore compressibility calculation. The pore compressibility from these three measurements are in good agreement. The compressibilities calculated from NMR, SIP and CMS-300 are static data. Ultrasonic velocity measurements were conducted to determine the dynamic pore compressibility. A correlation between static and dynamic pore compressibility was established. Static measurement exhibits higher pore compressibility compared to the dynamic data. This correlation is usable to convert the dynamic acquired data into static data, especially for this formation. This acquired correlation can be used in geomechanical modeling of the reservoir behavior.

TABLE OF CONTENTS

LIST OF FIGURES

LIST OF TABLES

LIST OF ABBREVIATIONS

Nuclear Magnetic Resonance . . . . . NMR

Spectral Induced Polarization . . . . . SIP

Water Immersion Porosimetry . . . . . WIP

micro X-Ray Computed Tomography . . . . . μ-XCT

ACKNOWLEDGMENTS

I would like to express my gratitude to my advisor Dr. Manika Prasad for her support, patience, and immense knowledge during my research. Secondly, I would like to thank my thesis committee members Dr. Erdal Ozkan and Dr. Luis Zerpa for their support and insightful comments.

Additionally, I would like to thank Milad Saidian for the time he has spent teaching me NMR, Kurt Livo for helping me acquire the NMR data, Mandy Schindler for obtaining the CT images, and Azar Hasanov, Liwei Ou, and Cesar Mapeli for their input in my research.

I would also like to thank my friends and colleagues in the OCLASSH Consortium and Center for Rock Abuse. I am extending my gratitude to PE faculty staff Denise Winn-Bower and Terri Snyder for their support and assistance.

Finally, I would like to thank my family and friends, for their constant support and encouragement.

CHAPTER 1

INTRODUCTION

Pore volume compressibility is an important property in reservoir simulation. During the production of oil&gas reservoirs, the pore pressure decreases, and the effective pressure increases due to constant overburden pressure. This results in pore compression due to reservoir compaction. Pore volume compressibility needs to be considered during reservoir characterization, because the compression of the pores will affect the porosity of the formation and this can lead to miscalculation of recoverable hydrocarbon volume.

The pore volume compressibility can be determined by the dynamic measurement approach, by calculating it from the logging data and ultrasonic measurements. However, dynamic pore volume compressibility underestimates the compressibility value due to the existence of micro-cracks (Geertsma, 1957). Therefore, static pore volume measurement is required, as it is more representative of the actual reservoir property. Both the static and dynamic measurements are conducted under drained conditions, in this case the sample being dry or saturated will not affect the acquired data. The static and dynamic measurements differ from one another by the frequency of deformation. The dynamic measurements are run with high frequency and low amplitude, and this results in insufficient time for the fluids inside the system to stabilize and also the rock appears to be stiffer with the increase in frequency of the applied stress. However, the static measurements are run with lower frequency and the measurements are acquired after the fluid has stabilized. The difference between the static and the dynamic measurements decrease as the confining pressure increases; this can be related to the closure of low-aspect ratio pores (Geertsma 1957).

In this study, pore compressibility was determined using the low-field, 2 MHz, Nuclear Magnetic Resonance (NMR) apparatus. The acquired data from the NMR were converted from time domain to size domain using the surface relaxivity values taken from the literature (Marschall et al. 1995). The pore size distribution acquired from NMR were checked against the Spectral Induced Polarization (SIP) – low-frequency electrical conductivity measurement to verify the used surface relaxivity values. Analysis of porosity and permeability changes under varying confining pressures was conducted for these samples. This work investigates the static pore compressibility from the NMR response under a maximum confining pressure of 10 MPa and the static pore compressibility from the SIP and Helium porosity for confining pressure of 17 MPa. Calculation of dynamic pore space compressibility from the acoustic measurements was used to find the correlation between the static and dynamic pore volume compressibilities. The static and dynamic pore compressibility correlation is required to convert the dynamic data acquired from the field to more required static data, and this correlation can be used for geomechanical modeling of the reservoir behavior.

1.1 Motivation

The motivation for conducting high pressure experiments and looking at pore compressibility calculations from this data was mainly due to the work conducted by Azar Hasanov in his master's thesis (Hasanov 2014). In the study, pre-and post-pressurization of the San-Andres Dolostone sample was observed. The experiment was conducted up to a maximum pressure of 69 MPa. The pre-and post-CT scans, and the NMR measurements were run. From the comparison of CT images before and after the hydrostatic loading, significant pore collapse and grain crushing can be observed in Figure 1.1. Pore collapse results in reduction of porosity and increase in stiffness of the rocks.

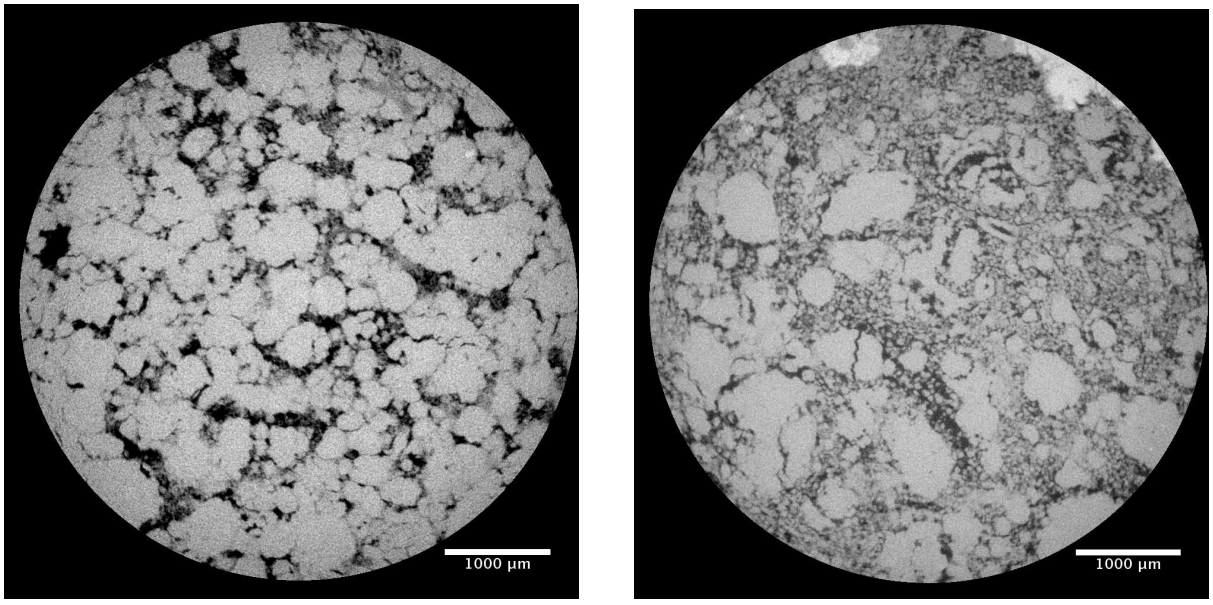

(a) San-Andres sample pre-pressurization. (b) San-Andres sample post-pressurization.

Figure 1.1: μ-CT scan for San-Andres sample, before and after the hydrostatic loading experiment. Significant pore collapse and grain crushing can be observed (taken from Hasanov (2014)).

This result can also be seen in the NMR T_2 distribution measurements. Figure 1.2 corresponds to the experiment conducted before and after hydrostatic loading. From the figure collapse of larger pores (pores larger than 20 ms), and an increasing number of smaller pores can be observed.

1.2 Geological background

The samples for this study were provided from the Hibernia oil field, which is located 315 km east-southeast of the Grand Banks of St. John's Newfoundland, and is the largest oil field discovered on the eastern continent of North America (Brown et al. 1989). The Hibernia oil field is located in the Jeanne D'Arc basin (Figure 1.3).

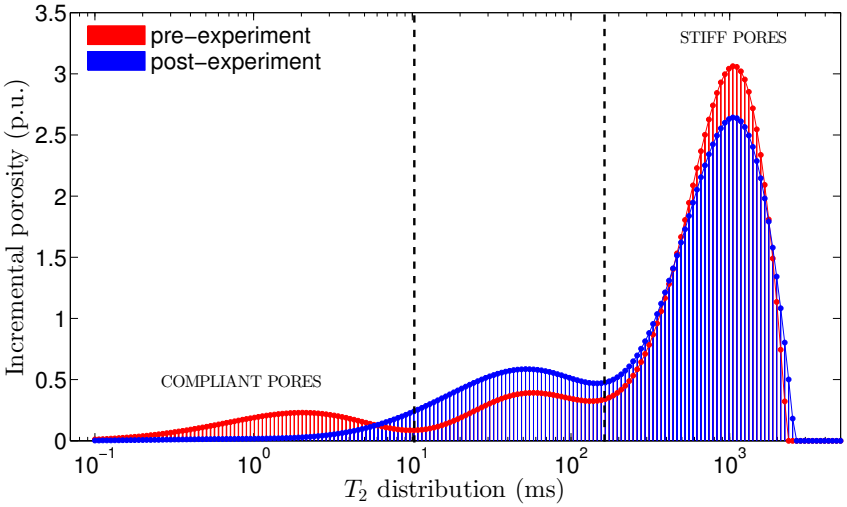

Figure 1.2: NMR T_2 distribution pre-and post-pressurization for San Andres dolostone sample. Pore collapse for larger pore, and increase in number of smaller pores can be observed (taken from Hasanov (2014)).

Two main reservoirs exist within the Hibernia oil field, the Hibernia reservoir and the Ben Nevis- Avalon reservoir. The Ben Nevis-Avalon reservoir is the shallower reservoir, a Cretaceous primary reservoir composed of the Barremian-Albian age river delta sandstones occurring at the depth of 2,100-3,000 m subsea and the Hibernia reservoir, composed of the Berriasian-Valanginian age sandstones, is the deeper of the two reservoirs, occurring at depths between 3,475-4,200 m subsea (Figure 1.4) (Brown et al. 1989).

1.3 Literature review

The compressibility of reservoir rocks has been well studied by a number of researchers using different methods. Carpenter and Spencer (1940) are the earliest reported researchers, who attempted to measure the compressibility of reservoir rocks. They conducted compressibility measurement on consolidated oil-bearing sandstones collected from east Texas. Hall (1953) studied pore compressibility change under constant confining pressure and variation in pore pressure for limestone and sandstone samples. The compressibility was calculated from the change in pore volume, which was determined using a gauge. Hall (1953) developed an empirical correlation between pore compressibility and porosity. The observed pore compressibility ranges between 3×10^{-6} to 10^{-7} psi^{-1}, and he determined that ignoring compressibility can lead to overestimation of oil in place by 30% to 40%. Fatt (1958) conducted a similar experiment to Hall (1953); however, he conducted the measurement under higher confining and pore pressures. Fatt (1958) determined that pore compressibility can not be correlated using porosity and is a function of pressure. Zimmerman et al. (1986) developed a relationship for rock compressibility from confining and pore pressure, and verified his relationship by conducting experimental measurements on sandstone samples. Poston and Chen (1987) used the material

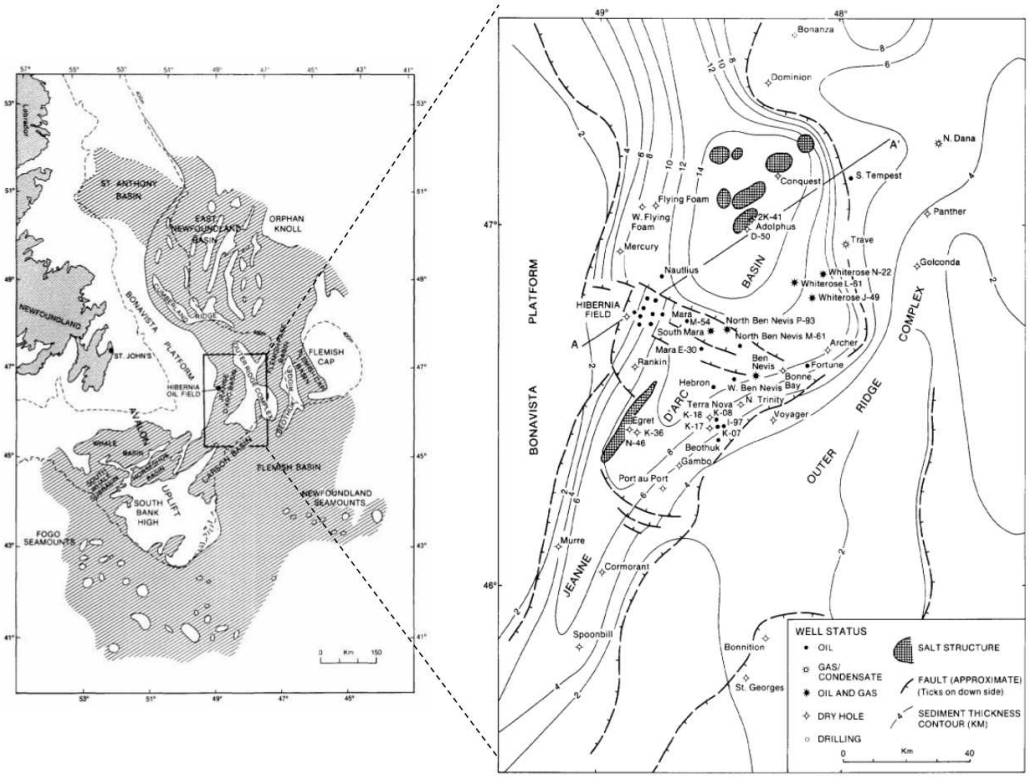

Figure 1.3: Hibernia oil field located in Jeanne D'Arc basin (Brown et al. 1989).

balance to determine the formation compressibility and gas in place. Macini and Mesini (1998) determined the pore compressibility of sandstone and limestone samples for both static and dynamic measurements. The static measurement was conducted using the deformation test, and the dynamic pore compressibility was determined from the acoustic measurement. Yildiz (1987) used the production data to predict the pore compressibility. Marchina et al. (2004) studied compressibility of heavy oil rocks. The study was conducted similarly to Hall (1953) and Fatt (1958), by looking at the change in displaced fluid using the dilatometer device. Li and Du (2004) calculated the compressibility using the Poisson's ratio, and elastic modulus. Suman (2009) estimated the compressibility using the sonic velocity derived from the seismic data.

The purpose of this work is to study pore compressibility using a new approach which has not been studied extensively. In this study, pore compressibility of sandstone samples were measured under elevated net confining pressure conditions using the NMR response. Li et al. (2013) was the only researcher who has published pore compressibility study using high pressure NMR for determining the stress sensitivity of pores for different ranks of coals. The experiment was conducted with 20 MHz NMR machine, up to maximum pressure of 10 MPa. The work was based on observing the change the coal had induced in the pores and fracture structure, under stress loads.

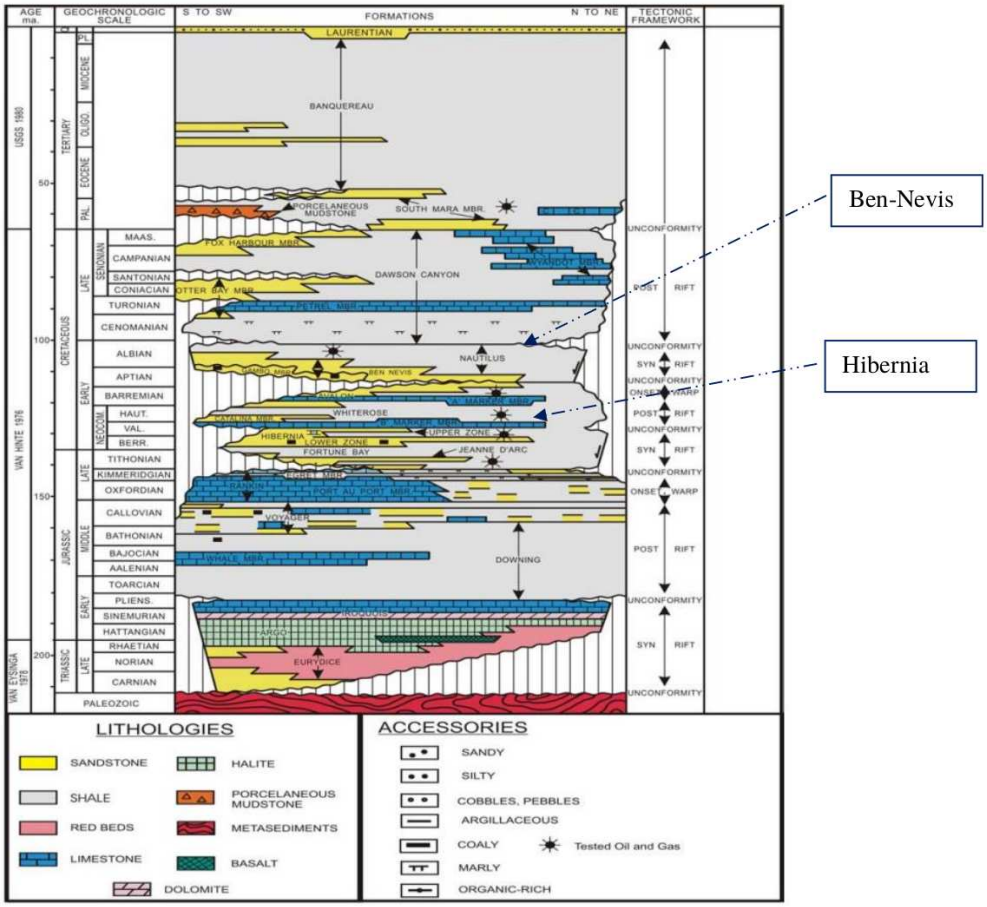

Figure 1.4: General stratigraphy of Jeanne D'Arc basin (Brown et al. 1989).

1.4 Research objective

The objective of my work is to determine if NMR is reliable option to determine the total pore compressibility. The accuracy of the NMR pore compressibility was clarified by comparing the results with the compressibility obtained from the SIP and helium porosity. The other objective of this study, is to investigate the NMR pore compressibility by discrete pore sizes, determine the relationship between the porosity and pore compressibility, and develop correlation between static pore compressibility (acquired from NMR, SIP, and helium porosity) and dynamic pore compressibility (acquired from acoustic) measurements. To achieve these goals, the following tasks were fullfilled:

- Comparing pore space compressibility using NMR, Helium porosity and electric conductivity. Determine if NMR is reliable option to measure pore compressibility.
- Determine which pores are mainly affected by compaction.

- Determine relationship between porosity and pore compressibility.
- Comparing the static and the dynamic pore compressibility.

1.5 Thesis organization

Here I provide a chapter-by-chapter overview of my thesis:

- Chapter 1 contains the motivation, introduction, literature review, and objective of my research.
- Chapter 2 describes laboratory procedure of various experiments and detailed description of methods used to calculate the pore space compressibilities.
- Chapter 3 presents the direct results of different laboratory experiments.
- Chapter 4 contains the discussion of observed correlations and trends.
- Chapter 5 provides conclusion of this study and suggests future works to be performed.

CHAPTER 2

MATERIALS AND METHODS

Core data acquired from Hibernia oil field, located in Jeanne D'Arc basin east-southeast of Grand Banks of St. John's Newfoundland, and Berea sample was used in this study. Using the core plugs, I measured nuclear magnetic resonance (NMR), helium porosity and permeability, spectral induced polarization (SIP), and ultrasonic velocities under confining pressure. More detailed information about the core plugs will be discussed in the material section. In the method section, detailed description of nuclear magnetic resonance (NMR), helium porosity and permeability, spectral induced polarization (SIP), and ultrasonic velocity measurement techniques and pore compressibility calculation will be explained.

2.1 Materials

In this study, eighteen core plugs were provided from two reservoirs (Hibernia and Ben-Nevis reservoir) located within the Hibernia oil field. Additionally, a Berea sample was studied for comparison purposes. Eighteen core plugs provided for two reservoirs consist of twelve cores from Hibernia reservoir, and six core plugs from Ben-Nevis reservoir. The cores belong to Cretaceous age sandstone formations. Figure 2.1 presents fourteen core samples provided for Hibernia and Ben-Nevis reservoir. From the overall images, samples with lighter color have higher quartz mineral composition. The F1 sample shown in Figure 2.1 is unconsolidated and poorly cemented. A Berea core was chosen as a standard benchmark sample for comparison. Berea sample with diameter of 1.5 inches and length of 2 inches was used for ultrasonic velocity, and spectral induced polarization (SIP) measurement. The ultrasonic velocity measurement, and spectral induced polarization (SIP) measurement was done at 17 MPa effective stress condition. The measurement was conducted using the PLP (Panfiloff–Larson–Prasad) jacket (Panfiloff 2016).

Minerology, porosity, and ultrasonic velocity data for eighteen Hibernia oil field samples was provided (courtesy of Manika Prasad) up to 60 MPa confining pressure. The core plugs have diameter of 1 inch and length of 1.2 inches. CMS-300 helium porosity and permeability measurement up to 10 MPa confining pressure was run on ten samples to determine the permeability, and to double-check the provided porosity values. Ultrasonic velocity measurement was not run on Hibernia oil field samples, because the PLP jacket requires samples with 1.5 inches in diameter and 2 inches in length.

Benchtop nuclear magnetic resonance (NMR) T_2 measurement was run on the thirteen Hibernia oil field samples. From the benchtop NMR measurement, and from the helium porosity and permeability data, three samples with variation in porosity and permeability values were chosen for high pressure NMR experiment.

Figure 2.1: 14 core samples for Hibernia and Ben-Nevis formation. The samples have different colorization depending on the mineral composition, samples with lighter color have a high percentage of quartz. The images show different grain size distribution and cementation of the core which affect the pore space.

Berea sample acquired from the same outcrop used for ultrasonic velocity measurement was also used in high pressure NMR experiment. The three samples chosen for high pressure NMR experiment are H1, J1, and 23A. μ-CT scans were run on these four samples to determine the pore distribution, pore shape and fracture propagation.

2.2 Methods

In this section, pore compressibility calculation and methodology for nuclear magnetic resonance (NMR), high pressure NMR, helium injection porosity and permeability, ultrasonic measurement under different confining pressure conditions will be discussed in detail. Table 2.1 presents the available and conducted measurement on provided samples.

2.2.1 Nuclear magnetic resonance

The hydrogen nucleus, consisting of a positive charged proton, has angular momentum (magnetic moment) caused by the spin in its axes, which acts as a bar magnet, Figure 2.2 (a). This principal is not only associated with hydrogen nucleus, any nucleus with odd number of neutrons or protons or both can behave as magnets (Coates et al. 1999). In the absence of external magnetic field, hydrogen nuclei spin axes are randomly oriented, as shown in Figure 2.2 (b) (Coates et al. 1999).

Table 2.1: List of samples, data and data source. ✓– measured, X – not measured, ∗ – data provided by Dr. Manika Prasad.

Sample	Acoustic	NMR	XRD	NMR + acoustic under pressure	ϕ	k	CMS-300	μ-CT	Electrical conductivity
A1	∗	✓	∗	X	∗	✓	✓	✓	X
B1	∗	✓	∗	X	∗	✓	✓	✓	X
H1	∗	✓	∗	✓	∗	✓	✓	✓	X
M1	∗	✓	∗	X	∗	✓	✓	✓	X
C1	∗	✓	∗	X	∗	✓	✓	✓	X
D1	∗	✓	∗	X	∗	✓	✓	✓	X
G1	∗	✓	∗	X	∗	✓	✓	✓	X
F1	X	✓	∗	X	∗	✓	X	✓	X
J1	∗	✓	∗	✓	∗	✓	✓	X	X
J2	∗	✓	∗	X	∗	✓	✓	X	X
K1	X	✓	X	X	✓	✓	✓	X	X
K2	X	✓	X	X	✓	✓	✓	X	X
23A	∗	✓	∗	✓	∗	✓	✓	✓	X
26A	∗	✓	∗	X	∗	✓	✓	✓	X
71A	∗	✓	∗	X	∗	✓	✓	✓	X
65A	∗	X	∗	X	∗	X	X	X	X
92A	∗	✓	∗	X	∗	✓	X	✓	X
99A	∗	X	∗	X	∗	X	X	X	X
Berea	✓	✓	X	✓	✓	✓	✓	X	✓

When an external magnetic field (static magnetic field, B_0) is applied, the randomly oriented hydrogen nuclei in pore space align in the direction of the magnetic field by the process called polarization. During polarization, the spinning nuclei precess (perpendicular to static magnetic field) around static magnetic field due to the angular momentum of the nuclei. The precession frequency is known as Larmor frequency (Coates et al. 1999).

The magnetic field, generated by strong magnet align the spinning protons parallel (low energy state) or anti-parallel (high energy state) to the primary coil, or mainly known as longitudinal direction (Coates et al. 1999). The number of spinning nuclei in low energy state are more than spinning nuclei in higher energy state, and the difference of these two results in net magnetization M_0.

2.2.1.1 T_1 - longitudinal relaxation time

Longitudinal relaxation time, T_1, is measurement conducted during the polarization of the nuclei to the static magnetic field, B_0. The nuclei spin axis aligns parallel or anti-parallel to the static magnetic field, with precession in the direction of B_0. The longitudinal relaxation time T1 is the length of time required for these randomly oriented nuclei to align with the applied magnetic field. The longitudinal relaxation time is

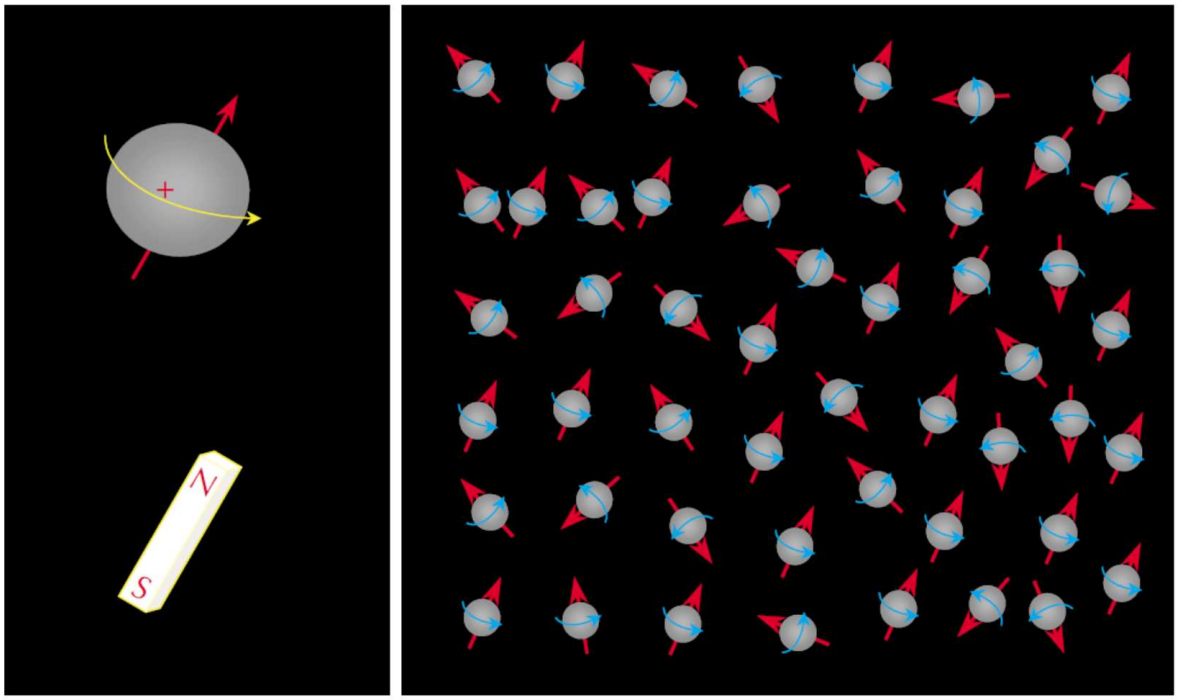

Figure 2.2: Hydrogen nuclear spin axes acts as a bar magnet; random orientation of hydrogen nuclei in the absence of external magnetic field (Coates et al. 1999).

depicted in Equation 2.1 and Figure 2.3:

$$M_z(t) = M_0 \left(1 - e^{-\frac{t}{T_1}}\right) \ , \tag{2.1}$$

where t is the time that static magnetic field is applied to the nuclei, $M_z(t)$ is the magnitude of magnetization at the time t, and M_0 is maximum magnetization at a given magnetic field.

Longitudinal relaxation time in porous media is controlled by two type of relaxation mechanisms. Surface relaxation, where protons are in contact with the rock surface. And, Bulk fluid relaxation, where protons are free floating in the pore away from the pore surface. These two type of relaxation mechanisms take place in the same time, however, they vary in their magnitude of the relaxation time. This allow them to be differentiated. The longitudinal relaxation time is expressed as follows:

$$\frac{1}{T_1} = \frac{1}{T_{1,bulk}} + \frac{1}{T_{1,surface}} \ , \tag{2.2}$$

where T_1 is longitudinal relaxation time, $T_{1,bulk}$ is the bulk fluid relaxation, and $T_{1,surface}$ is the surface relaxation.

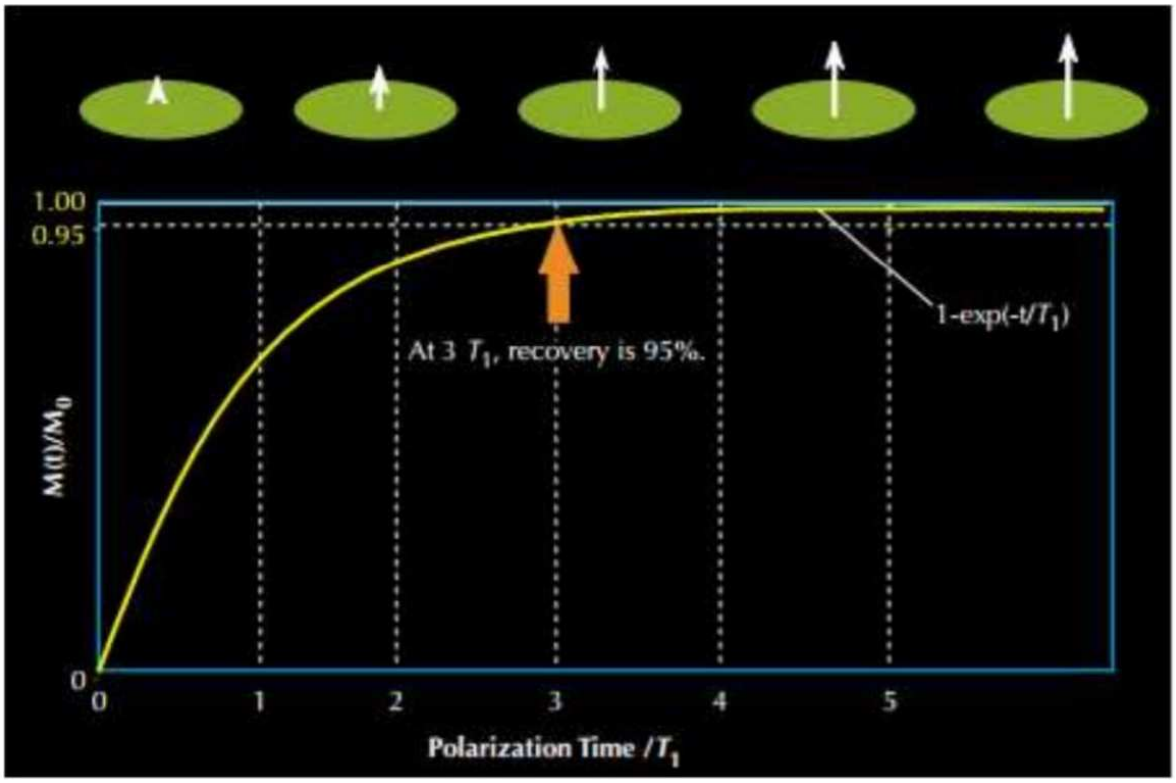

Figure 2.3: Polarization curve of hydrogen nuclei in longitudinal direction by the application of static magnetic field (Coates et al. 1999).

2.2.1.2 T_2 - transverse relaxation time

Transverse relaxation time, T_2 is the most important NMR experiment, which allows more deeper understanding into pore properties. Transverse relaxation time experiment is conducted by tipping the nuclei spin axis perpendicular to the longitudinal direction. The polarized hydrogen nuclei in the direction of static magnetic field, B_0 are tipped perpendicular (90°) or anti-perpendicular (180°) by application of secondary stronger magnetic field (oscillating magnetic field), B_1. The measurement of the decay from the secondary magnetic field to initial static magnetic is the transverse relaxation time, T_2.

Transverse relaxation time, T_2 in porous media is controlled by relaxation mechanisms similar to Longitudinal relaxation time, T_1. Compared to T_1 relaxation time, T_2 relaxation time is not only affected by bulk fluid and surface relaxation, but also diffusion relaxation mechanism. The transverse relaxation time is expressed as follows:

$$\frac{1}{T_2} = \frac{1}{T_{2,bulk}} + \frac{1}{T_{2,surface}} + \frac{1}{T_{2,diffusion}} \ , \tag{2.3}$$

where T_2 is the transverse relaxation time, $T_{2,bulk}$ is the bulk fluid relaxation, $T_{2,surface}$ is the surface relaxation, and $T_{2,diffusion}$ is the diffusion relaxation.

Diffusion relaxation mechanism is the molecular diffusion of nuclei in pore fluid. Diffusion take place very quick in large pore space and is not detectable by the low-field NMR machine that is used in this research (Saidian 2015). Due to fast diffusion relaxation and slow bulk relaxation, the transverse relaxation time can be expressed with surface relaxation mechanism:

$$\frac{1}{T_2} = \frac{1}{T_{2,surface}} = \rho_2 \frac{S}{V} \ , \tag{2.4}$$

where $T_{2,surface}$ is the surface relaxation time, ρ_2 is the surface relaxivity, S is the rock surface area, and V is the pore volume.

2.2.1.3 Determining the pore size distribution from the transverse relaxation time

The pore size distribution of rock sample fully saturated with water is acquired from the inverted magnetic decay signal collected during the T_2, transverse relaxation time. The acquired data is converted to time domain by using the Laplace transformation.

An important part of NMR study is converting the acquired transverse relaxation time, T_2 distribution from time domain, into the size domain. Determining the surface relaxivity value (ρ) is important for converting the T_2 distribution from time domain to the size domain. Surface relaxivity value depends on the formation type.

There are three methods for determining the surface relaxivity value. The first method is the comparison of pore size distribution obtained from NMR, with other methods such as mercury intrusion, or nitrogen adsorption. (Figure 2.4) shows pore size distribution comparison from NMR and mercury intrusion. As seen in Figure 2.4, effective surface relaxivity (ρ_e) is applied to the mercury intrusion curve to match it with NMR curve (Coates et al. 1999).

Second method is by calculating the surface relaxivity value directly from nitrogen adsorption or image analyses, and the T_2 relaxation time as shown below (Dunn et al. 2002):

$$\rho = T_2^{-1} \frac{S}{V} \ , \tag{2.5}$$

where ρ is the surface relaxivity, T_2 is the transverse relaxation time, S is the pore surface are, and V is the pore volume. The last method is from the diffusion experiment. However, this measurement is not always applicable for every rock type, because this measurements are time consuming and require intense measurement.

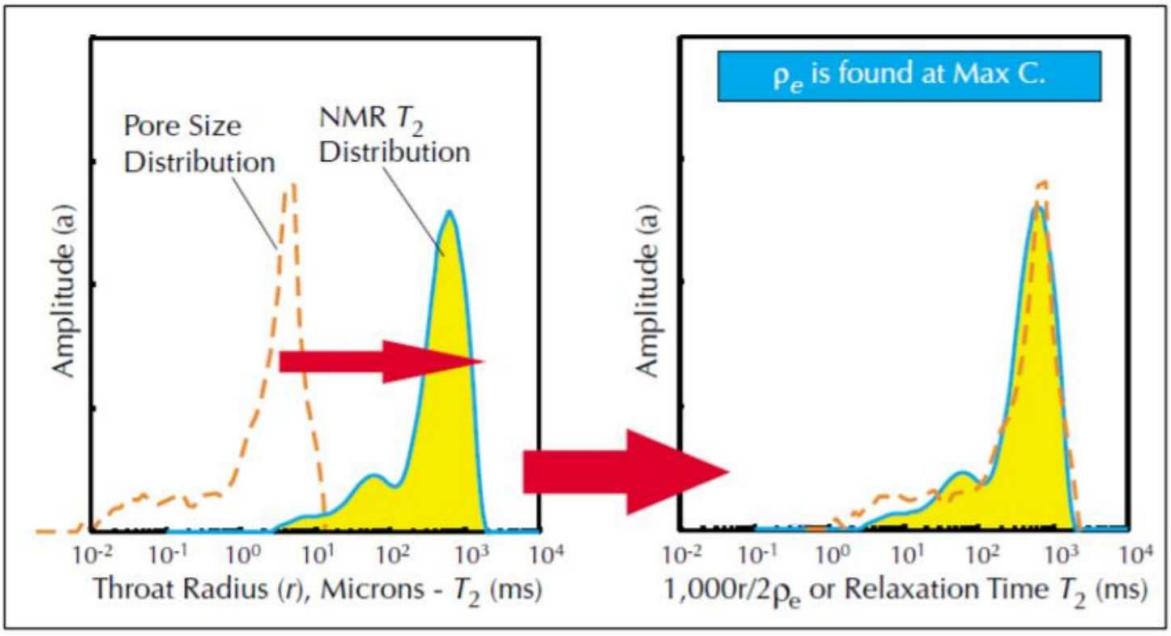

Figure 2.4: Comparison of pore size distribution acquired from NMR and Mercury intrusion (Coates et al. 1999).

2.2.2 Nuclear magnetic resonance from NMR measurements

For these experiments, a 2 MHz $Magritek^{TM}$ NMR rock core analyzer was used to measure the transverse relaxation time (T_2) signal. This device has the capability of measuring both the longitudinal and transverse times and the create 2D correlation maps. The T_2 relaxation time is a result of mathematical inversion of the decay time, based on fluid types and properties of the porous material such as pore size distribution and wettability (Coates et al. 1999). The purpose of these measurements was to determine pore size distribution and the porosity of the samples. The T_2 relaxation data were acquired for 17 fully brine saturated samples (Table 2.1) from Hibernia and Ben-Nevis formations at ambient pressure and temperature conditions. The core plugs, with diameter of 1 inch and length of 1.4 inch, were cleaned using the Soxhlet extraction instrument with a methanol solution to remove impurities in the cores, vacuum oven dried under temperature of 80° C for 24 hours, and vacuum saturated with 2000 ppm brine solution made from NaCl, and distilled water for 24 hours to reach equilibrium. After the saturation, the cores were kept submerged in the solution for two days to achieve full saturation.

The sample was placed inside the plastic container to reduce the moisture loss during the NMR experiment. Before the experiment, the plastic container was separately run in NMR machine to acquire the background correction. The background correction was imported into the program to decrease the induced noise error, which can result in overestimation of the sample amplitude and lead to overestimation of core

porosity. The experiment was run to constrain the experimental parameters (inter-experimental delay of 7500 ms, echo time of 100 s, number of echoes between 7500-20000, minimum signal to noise ratio of 150-200) to ensure all the spectrum is acquired. The NMR relaxation mechanism consists of three independent relaxation variables. These include bulk fluid relaxation ($T_{1,bulk}$ and $T_{2,bulk}$), surface relaxation ($T_{1,surface}$ and $T_{2,surface}$), and diffusion ($T_{2,diffusion}$) (Coates et al. 1999). Transverse relaxation time T_2 is expressed in Equation 2.3.

Bulk, surface, and diffusion indices refer to relaxation times to the effect of bulk fluid, grain surface and molecular diffusion in the presence of a primary magnetic gradient. Bulk fluid relaxation is small, and diffusion relaxation occurs on longer time scale, so the NMR relaxation is assumed to rely solely on surface relaxation.

2.2.3 High pressure NMR experiment

High pressure NMR experiments were performed using a pressure vessel specifically made for NMR from Torlon plastic material (courtesy of Kurt Livo and Matthias Pohl). A solid cylinder with 2 inches outer diameter was drilled to create an inner bore of 1 inch (courtesy School of Trades). The open end was covered with a 2 inch diameter Swagelok end cap which contains electrical and hydraulic connections (courtesy of Matthias Pohl).

Four samples were measured, one virgin Berea sample and three samples were chosen from Hibernia and the Ben-Nevis formations depending on their variety of porosity (J1–11.84%, H1–20.69%, 23A–23.9%) to see the change in pore space compressibility. The cores were cut down to 0.9 inches in diameter and length of approximately 1.4 inches. The samples were cleaned using Soxhlet extractor with methanol for two days to remove salt and other impurities, vacuum oven dried with temperature of 120° C for 24 hours and vacuum saturated with brine solution of 0.01 mol/l of NaCl for 24 hours, and kept submerged for 4-5 days.

The core was isolated from sides using polyolefin heat shrink tube and plastic end caps with piezoelectric crystals (compressional and shear) imbedded into them (Figure 2.5). Confining pressure was created using research grade (99.99% pure) Nitrogen gas with pressure steps of 3.5 MPa and maximum achieved pressures of 10 MPa. The pore pressure was kept at ambient pressure conditions. Piezoelectric crystals at the end caps allowed acquisition of the acoustic measurements at each pressure step.

The jacket was put together without the core, and the background correction was run to decrease the noise error caused by the plastic sealing, metallic pipes, wires and piezoelectric crystals. The porosity values at each pressure steps were determined using CMS-300 (helium porosimetry), and the calculated bulk volume was used in the NMR program to normalize the signal. The porosity for ambient condition was measured using water immersion porosimetry (Kuila 2013). The NMR high pressure measurements were

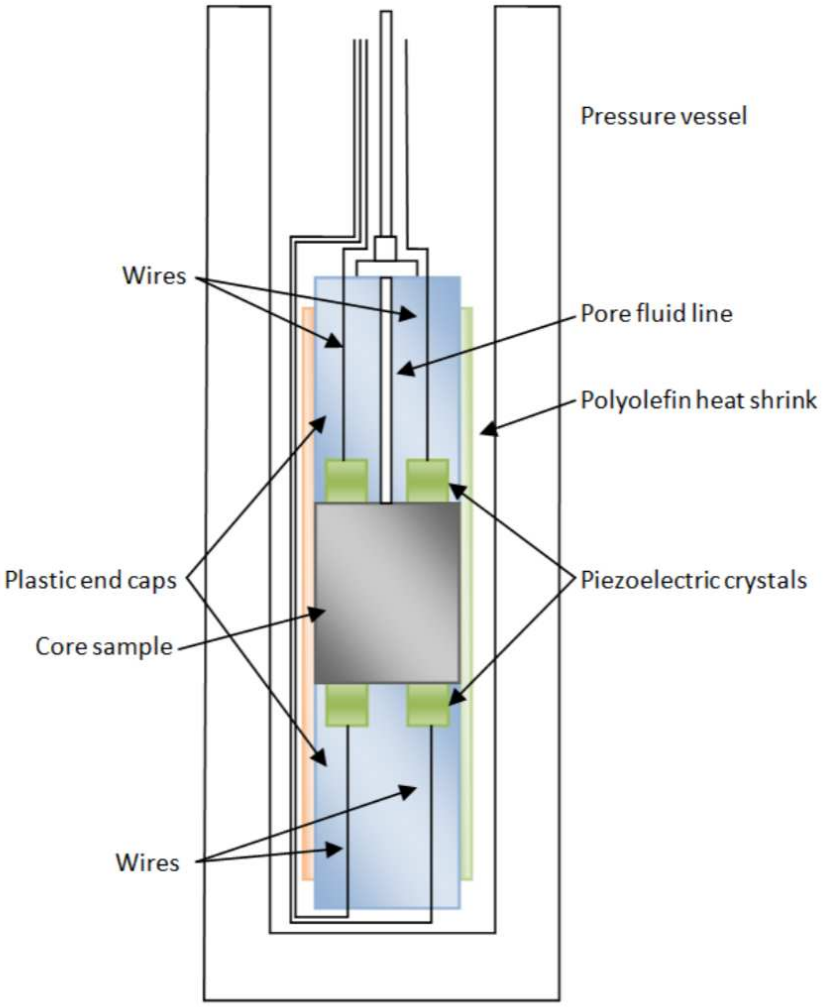

Figure 2.5: Experimental schematics for high pressure NMR and ultrasonic experiment.

run at experimental parameters of inter-experimental delay of 1000-4000 ms, echo time of 100 μs, number of echoes between 5000-9000, minimum signal to noise ratio of 100.

2.2.4 Pore size distribution from NMR measurements

The more conventional way of determining pore size distribution is by using mercury injection measurements. Pore size distribution can also be determined using the T_2 relaxation time, effective surface relaxation S and pore surface-to-volume ratio ($\frac{S}{V}$), (Marschall et al. (1995) and Coates et al. (1999)):

$$\frac{1}{T_2} = \rho \left(\frac{S}{V} \right). \tag{2.6}$$

By assuming that the pores are cylindrical, pore surface-to-volume ratio can be equal to 2/r, and the pore radii can be calculated from T_2 values.

$$T_2 = \frac{1000r}{2\rho}. \tag{2.7}$$

Surface relaxation is found from literature Marschall et al. (1995). Using the XRD data the effective surface relaxation can be determined by:

$$\rho_{aver} = \rho_1 V_1 + \rho_2 V_2 + \cdots + \rho_n V_n, \tag{2.8}$$

where ρ_{aver} is the average surface relaxivity of the given core samples, ρ_1, ρ_2, ρ_e is effective surface relaxation depending on mineralogy, and V_1, V_2, V_n is a volume percentage of each mineral.

Hibernia samples are mainly consisted of quartz minerals, from this it can be assumed that the effective surface relaxation to be between 6.42 to 23 μm/s, an average of 16 μm/s. By placing the effective surface relaxation Equation 2.8 into the Equation 2.7 we can calculate the pore radius (Coates et al. 1999).

2.2.5 Ultrasonic velocity measurements

Ultrasonic velocity measurement is based on the principal of mechanical wave propagation through the given sample. The measurement was conducted using the PLP core holder (Figure 2.6). The core holder was developed by the collaboration of Dr. Manika Prasad, Larson Engineering, and Andre Panfiloff (Panfiloff 2016). The core holder grants simultaneous ultrasonic wave velocity and induced polarization measurement. The compressional (P) and the shear (S) waves can be measured at 0, 45, and 90 degrees according to the bedding of the sample. 1 MHz frequency piezoelectric crystals were used for the measurement. The rubber end caps are used for sealing, and the pore line embedded on each cap allows pore pressure regulation.

The system used in the experiment is composed of pressure generator (in my experiments Teledyne ISCO pump was used), pressure vessel limited to 69 MPa, PLP core holder with embedded piezoelectric crystals, and oscilloscope (for wave acquisition) (Figure 2.7).

The Teledyne ISCO pump was used for creating the necessary confining pressure inside the pressure vessel, hydraulic oil was used for creating pressure. The principal of wave acquisition is very simple. Two piezoelectric crystals are placed opposite to one another on the surface of the sample. The first piezoelectric crystal (transmitter transducer) converts the created electrical signal by a pulser into the mechanical wave, that propagates through the given sample. The secondary piezoelectric crystal (receiver transducer) opposite to the first crystal reconverts the propagating wave back to electrical signal. The signal is then processed as a wave (amplitude over time) by the oscilloscope and is recorded by the computer software.

In my experiment dry virgin Berea sample with diameter of 1.5 inches and length of 2 inches was used for ultrasonic velocity measurement. The sample was cored from the outcrop and cleaned for two days with

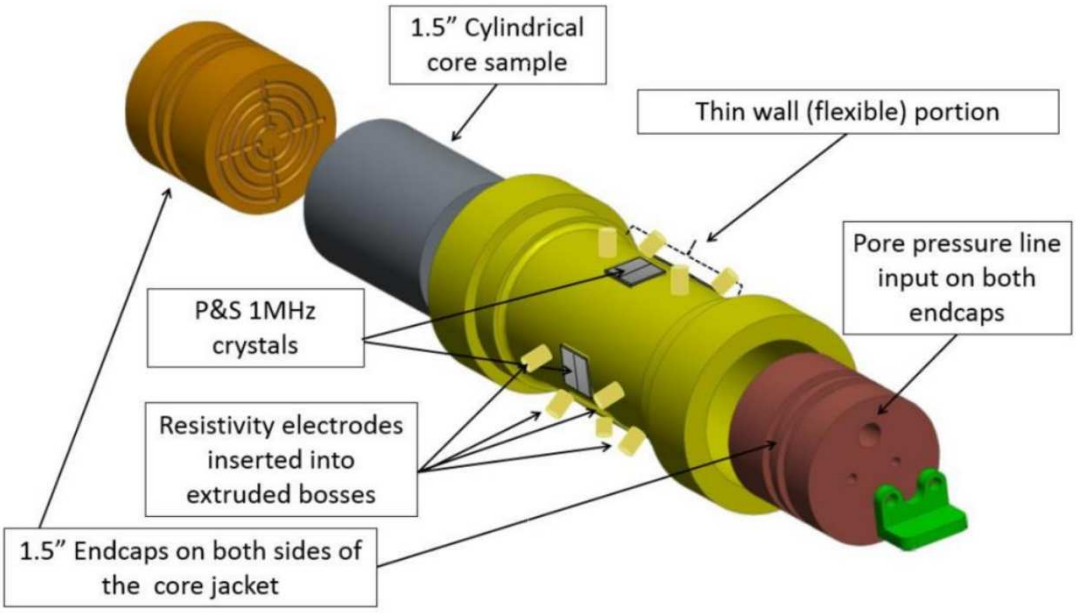

Figure 2.6: The PLP (Prasad–Larson–Panfiloff) core holder used for ultrasonic velocity and induced polarization measurement. The core holder grants ultrasonic measurement at 0, 45, and 90 degrees. The induced polarization is conducted using the four-electrode method. The end caps provide sealing and pore pressure control (Panfiloff 2016).

Soxhlet extractor, using methanol as the extracting fluid. The cores were then vacuum oven dried for 24 hours at temperature of 150 °C. The ultrasonic velocity measurement was conducted with 3.5 MPa pressure steps, up to maximum confining pressure of 17 MPa. The compressional and shear waves were measured at 0, 45, and 90 degrees according to the bedding plane. Benchtop ultrasonic velocity measurement was conducted pre- and post- pressurization. The velocity data was picked from the highest pressure down to the atmospheric pressure to see the irreversible damage.

The Figure 2.8 present compressional (P) and shear (S) waves acquired for the Berea sample at 17 MPa confining pressure. Ultrasonic wave velocity is determined using the following equation:

$$V = \frac{d}{t}, \tag{2.9}$$

where V is the acoustic velocity, d is the distance between the two opposite piezoelectric crystals (in this case the diameter of the sample), and t is the first arrival time for compressional (P) or shear (S) wave. As we can see from the Figure 2.8 the shear wave is slower compared to the compressional wave. The first arrival time for a wave is determined by the person analyzing the data and this can lead to error in the acquired velocity. Error propagation is required to determine the error margin of the acquired data.

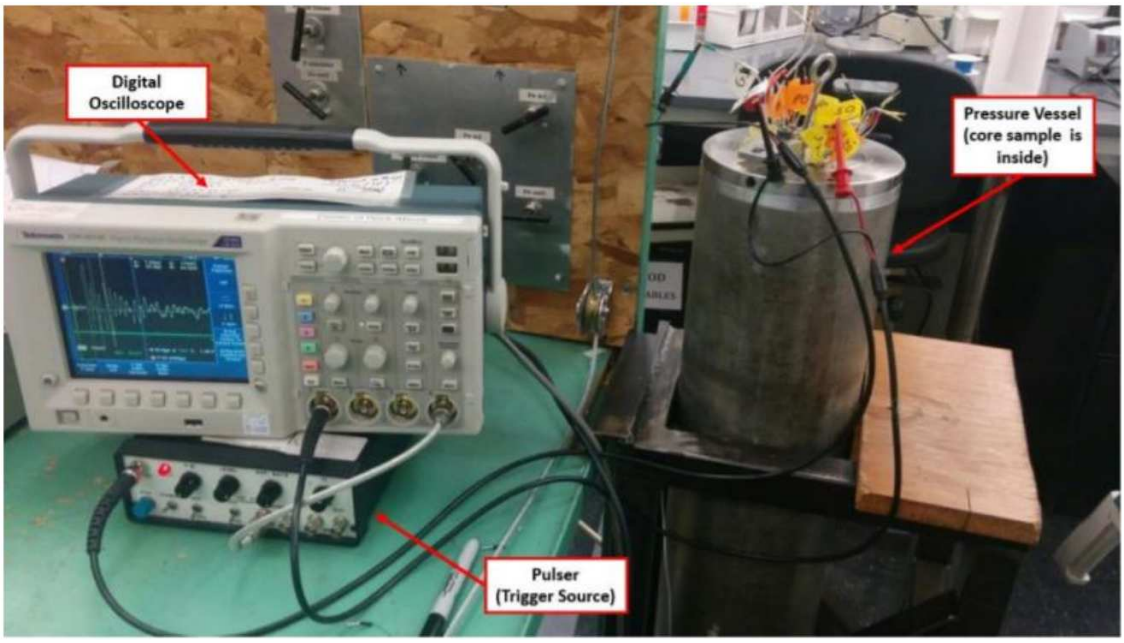

Figure 2.7: Setup used for ultrasonic velocity measurement under confining pressure. The setup consists of pulser (1 MHz frequency), oscilloscope for wave acquisition, pressure vessel limited to 69 MPa confining pressure, and PLP jacket located inside the vessel (Panfiloff 2016).

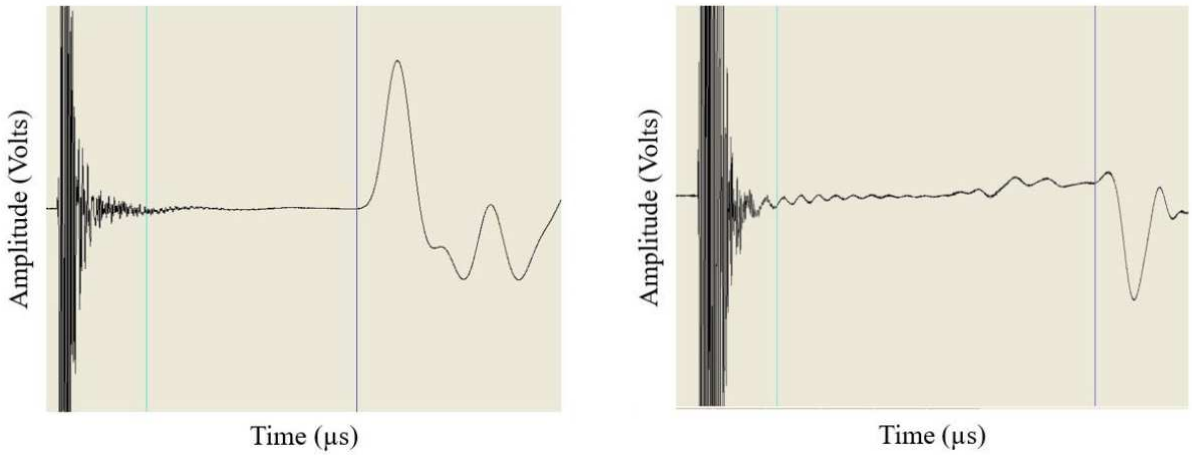

(a) Compressional (P) wave.

(b) Shear (S) wave.

Figure 2.8: Compressional and shear wave acquired for Berea samples at confining pressure of 17 MPa. Blue line indicates the first arrival time selected for each wave.

2.2.6 Simultaneous ultrasonic velocity, and induced polarization measurement

Ultrasonic velocity, and electric conductivity measurements in this part of the study were carried out simultaneously using the PLP core holder (Panfiloff 2016). The detailed explanation of ultrasonic velocity

measurement was provided in the previous section (2.2.5).

The purpose of using the electric conductivity is to determine the pore size distribution of the given sample under elevated pressure, and is based on the induced polarization in the core sample. The 4-electrode method was used for determining the induced polarization. The two electrodes placed on the end cap of the core holder creates the necessary current through the rock, and the two electrodes on the side of the core holder detect the voltage drop between the two points. The phase angle and the resistivity is determined by spectral induced polarization (SIP). The frequency used for the experiment was between 12 kHz to 1 MHz.

Purpose of this experiment is to interpret low-frequency polarization in porous media, and from quadrature conductivity of mineral materials that distribute the relaxation times, which can be related to pore size distribution of porous core samples.

The pore size distribution is determined

$$\tau = \frac{r^2}{2D^S_{(+)}} \tag{2.10}$$

$$\log_{10} r = \frac{1}{2}[\log_{10} \tau] + \log_{10}(2D^S_{(+)}) \tag{2.11}$$

where τ is the distribution of relaxation time determined from the measurements (Revil et al. 2014), $D^S_{(+)}$ denotes the diffusion coefficient of the counter ions in the Stern layer, and r is the pore size distribution.

The setup used for simultaneous ultrasonic velocity, and induced polarization measurement is similar to the setup explained in Section 2.2.5, with additional Teledyne ISCO pump, and transfer vessel to create pore pressure in the sample. The pore pressure of 0.7 MPa was sustained throughout the experiment to fully saturate the sample. Full saturation of the sample is required for electric conductivity measurement.

The experiment was carried out using the 1.5 inches in diameter and 2 inches in length virgin Berea sample. The sample was saturated with brine solution of 0.01 mol/l NaCl. The ultrasonic velocity, and induced polarization was measured up to maximum confining pressure of 17 MPa confining pressure, with pressure increments of 3.5 MPa.

2.2.7 Static pore compressibility calculation

The static pore compressibility as a function of the confining pressure is defined as:

$$C_p = -\frac{1}{V_p}\left(\frac{\partial V_p}{\partial P}\right)_{P_P} \tag{2.12}$$

where C_p is the pore compressibility at confining pressure, V_p is the pore volume at initial pressure, ∂V_p is the change in pore volume, and ∂P is the change in confining pressure. The negative term in the equation is to compensate the downward action of the external pressure.

2.2.8 Dynamic pore compressibility calculation

Dynamic pore compressibility for the Hibernia and Ben-Nevis data was calculated using Zimmerman's equation (Zimmerman et al. 1986):

$$C_{pc} = \frac{C_{bc} - C_r}{\phi} \tag{2.13}$$

$$C_{bp} = \phi * C_{pc} \tag{2.14}$$

$$C_r = C_{bc} - C_{bp} \tag{2.15}$$

where C_{pc} is the pore compressibility at confining pressure, C_r is the grain compressibility and depends on the composition of the grains, C_{bc} is the bulk compressibility at confining pressure, and C_{bp} is the bulk compressibility at pore pressure.

The C_{bc} and C_r parameters can be calculated using the formulas below:

$$C_{bc} = \frac{1}{K_{dry}} \qquad C_r = \frac{1}{K_{min}} \tag{2.16}$$

In this equation K_{dry} is the bulk modulus and K_{min} is the mineral bulk modulus. The dry bulk modulus for Berea sample was calculated from the ultrasonic velocities. The dry bulk modulus for Hibernia and Ben âĂŞ Nevis reservoir formation was provided (courtesy of Manika Prasad). The mineral bulk modulus can be determined by the VRH (Voigt-Reuss-Hill) average:

$$K_{Voigt} = f_1K_1 + f_2K_2 + \cdots + f_nK_n \tag{2.17}$$

$$K_{Reuss} = \frac{f_1}{K_1} + \frac{f_2}{K_2} + \cdots + \frac{f_n}{K_n} \tag{2.18}$$

where f_1, f_2, f_n are the volume percentage of each mineral and K_1, K_2, K_n are the mineral bulk modulus of each mineral.

$$K_{V\,RH} = \frac{1}{2}(K_{Voigt} + K_{Reuss}) \tag{2.19}$$

The simultaneous ultrasonic velocity and induced polarization measurement, provides us with saturated bulk modulus. The dry bulk modulus was calculated from the back calculation of Gassmann fluid substitution (Avseth et al. 2010). The Gassmann fluid substitution is as follows:

$$K_{sat} = K^* + \frac{\left(1 - \frac{K^*}{K_o}\right)^2}{\frac{\phi}{K_{fl}} + \frac{(1-\phi)}{K_o} - \frac{K^*}{K_o^2}} \tag{2.20}$$

where K_{sat} is the saturated bulk modulus, K_o is the mineral bulk modulus, K_{fl} is the bulk modulus of the pore fluid, K^* is the bulk modulus of the porous rock frame, and ϕ is the porosity of the rock.

2.2.9 Helium porosity and permeability

Helium porosity and permeability was measured using the CMS-300 apparatus. The CMS-300 apparatus is nondestructive method of determining the samples porosity and permeability. The apparatus uses the nitrogen gas for effective pressure. The porosity and the permeability of the cores were measured by injecting helium gas which provides fluid flow in the porous media.

The porosity of the sample is determined by Boyle's law. The Boyle's law is when the temperature is constant, the volume of the ideal gas mass varies inversely with the absolute pressure (API RP 40 1998). The porosimeter is first calibrated by reference chamber volume and fluid line volume (dead volume). The core plug is placed inside an elastomer sleeve and sealed with end stems. Confining pressure higher than 3.5 MPa is applied to the surface of the sleeve to confine the sample. The helium gas is first admitted to the porosimeter reference chamber, which has a known volume, and the pressure of the gas is recorded. The gas in the reference chamber is then vented into the void volume of the sample, and the pressure is recorded again (API RP 40 1998). The schematics of the porosimeter is shown in Figure 2.9. The pore volume is calculated by the modified Boyle's law, which is

$$V_P = \frac{V_r\left(\frac{P_1 Z_2}{P_2 Z_1} - 1\right) - V_\vartheta}{1 - \frac{P_a Z_2}{P_2 Z_a}} - V_d \tag{2.21}$$

where P_1 is the absolute initial reference volume pressure, P_2 is the absolute expanded pressure, P_a is the initial absolute atmospheric pressure in the sample, Z_1 is the gas deviation factor at P_1, Z_2 is the gas deviation factor at P_2, Z_a is the gas deviation factor at P_a, V_r is the gas reference chamber volume, V_p is the sample pore volume, and V_d is the system dead volume.

The permeability of the sample is determined by unsteady-state flow condition, by the pressure falloff gas permeameter (Jones 1972). The schematics of the setup is shown in Figure 2.10. The upstream gas chamber is connected to the sample holder, and can apply hydrostatic stress to a sample. The gas chamber and the sample that are filled with gas are connected to the outlet valve, which is vented to the atmosphere. After the chamber and the sample is filled with gas and thermal equilibrium is reached, the outlet valve is opened for pressure decay. After the pressure has decayed to about 85 percent of the fill pressure, the acquisition is commenced. The pressure at different intervals are collected (API RP 40 1998).

In this study, porosity and permeability of 11 core samples (Table 2.1) were measured starting from 3.5 MPa confining pressure. The Berea sample was measured to maximum of 17 MPa corresponding to the ultrasonic velocity and induced polarization measurement. Ten Hibernia oil field samples were measured to maximum pressure of 10 MPa. The measurement was conducted at pressure increment of 3.5 MPa.

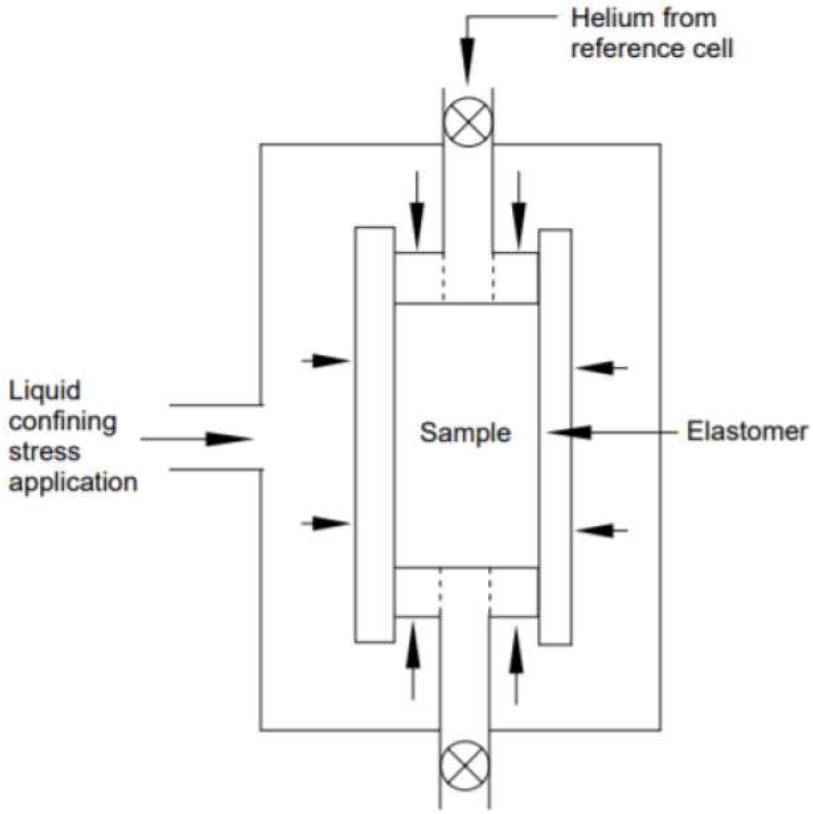

Figure 2.9: Schematic of isostatic load cell for direct determination of pore volume (taken from API RP 40 1998).

2.2.10 Water Immersion Porosimetry (WIP) measurement

Water immersion porosimetry (WIP) is based on the Archimedes principal. The WIP method was extensively researched by Utpalendu Kuila for measuring the porosity in gas shales (Kuila et al. 2014). The method can be used for determining porosity of sandstone samples.

In my study WIP method was used for determining the porosity of four samples (Berea, H1, J1, and 23A) before and after the helium porosity and permeability measurements. To conduct the WIP experiment, two chips of six grams in weight was cut for each sample pre – and post – experiment. The chips were vacuum oven dried under temperature of 150 Celsius for 24 hours. The dry weight of the chips was measured using the moisture analyzer, which heats the sample at 200 Celsius for 15 minutes before measuring the weight. After determining the dry weight, the chips were vacuum saturated with deionized (DI) water for two days. The sample were kept in the solution for five extra days to insure their full saturation.

The saturated chips weight in air and submerged in DI water were measured using the jolly balance set-up. The measurement for each chip was carried out five times and average value was calculated to remove

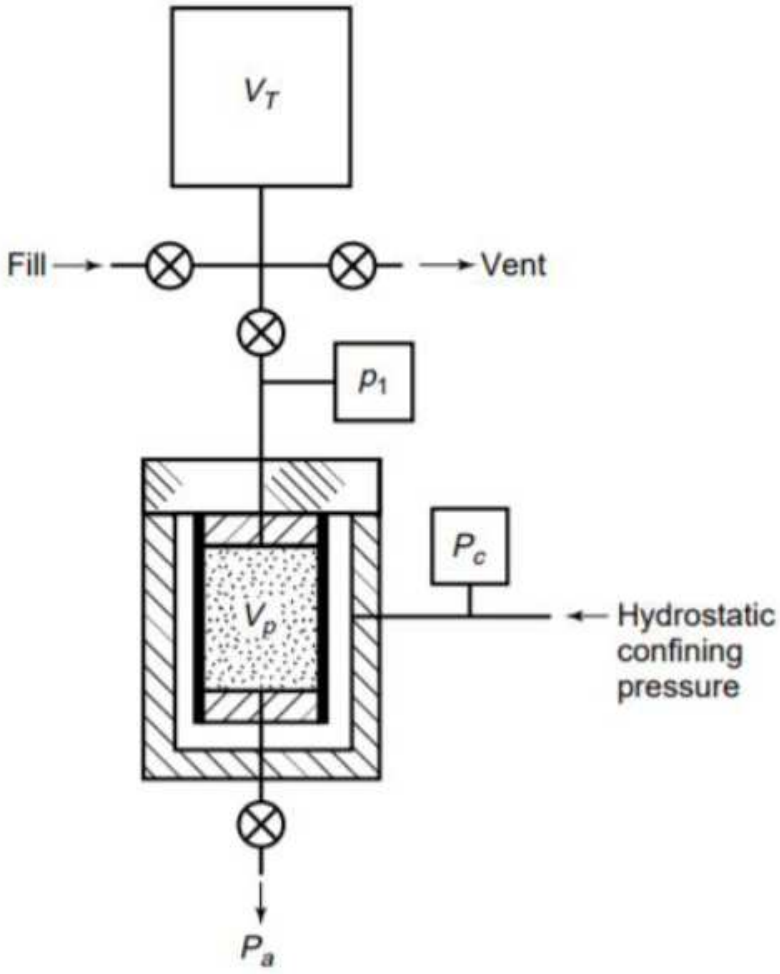

Figure 2.10: Schematic of pressure falloff gas permeameter (taken from API RP 40 1998).

the human error. The thermostat was placed inside the deionized water to calculate the fluid density.

The acquired weights for each chip are used to determine the water-saturated bulk density (ρ_B) and anhydrous grain density (ρ_G)

$$\rho_B = \left[\frac{SatWt_{air}}{SatWt_{air} - SatWt_{sub}} * (\rho_{H_2O} - \rho_{air})\right] + \rho_{air} \tag{2.22}$$

$$\rho_G = \left[\frac{DryWt_{air}}{DryWt_{air} - SatWt_{sub}} * (\rho_{H_2O} - \rho_{air})\right] + \rho_{air} \tag{2.23}$$

where, $DryWt_{air}$ is the dry weight of the chip, $SatWt_{air}$ is the saturated weight of the chip in air, $SatWt_{sub}$ is the saturated weight of the chip submerged, ρ_{air} is the density of the air, and ρ_{H_2O} is the density of the water depending on the temperature, which is calculated using the following equation:

$$\rho_{H_2O} = -0.0000053 * T^2 + 0.0000081 * T + 1.0001627 \tag{2.24}$$

where T is the temperature of the water during the measurement.

The WIP porosity of a sample is calculated using the following relationship:

$$\Phi_{WIP} = \frac{(\rho_B - \rho_G)}{(\rho_{H_2O} - \rho_G)} * 100 \tag{2.25}$$

2.2.11 Micro X-ray computed tomography

Micro X-Ray Computed Tomography (μ-CT) was performed (courtesy of Juliusz Radziszewski from Geophysics department) using Micro X-Ray Computed Tomography 400 apparatus acquired from XRadia with true spatial resolution of 0.7 μm and minimum achievable voxel size of 70 nm. Computed X-Ray tomography, or Micro CT, is a complete non-destructive method for examining the interiors of solid objects. It produces three-dimensional image revealing the interior of an examined object as if it had been cut open along the image plane for observing. X-Ray Computed Tomography relates to imaging of materials for determining mechanical and petrophysical properties. X-Ray CT scan helps better visualization and understanding of processes; for example, fracture, pore collapse, grain crushing, and so on (Hounsfield 1980).

The ImageJ software was used to analyze the μ-CT images. The image sequence (973 images scanned for each sample) was uploaded into the ImageJ software and 8 images from the sequence was chosen to determine the average porosity and the aspect ratio of the pores. The steps taken to determine the porosity and the aspect ratio is presented in Figure 2.11.

Figure 2.11(a) presents the image chosen to determine porosity and aspect ratio of the pores. The threshold value was chosen to separate the pore space from the grains (Figure 2.11(b)). After applying the threshold value, the image becomes binarized. The values below the threshold (the grains) become white and the pores, which are above the threshold become black (Figure 2.11(c)). The binarized image is processed through the particle analyzer module built in ImageJ software. The particle analyzer processes, and outlines the pores (Figure 2.11(d)). The table of results are created, which provide the porosity of the sample and the pore dimensions for each binarized pores. It is important to note that the threshold value was chosen by me, and accurate determination of the threshold depends on the quality of the image.

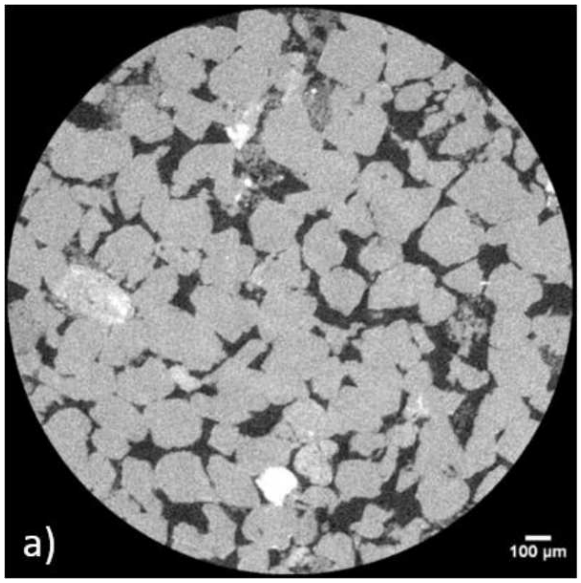

(a) Image chosen from the sequence.

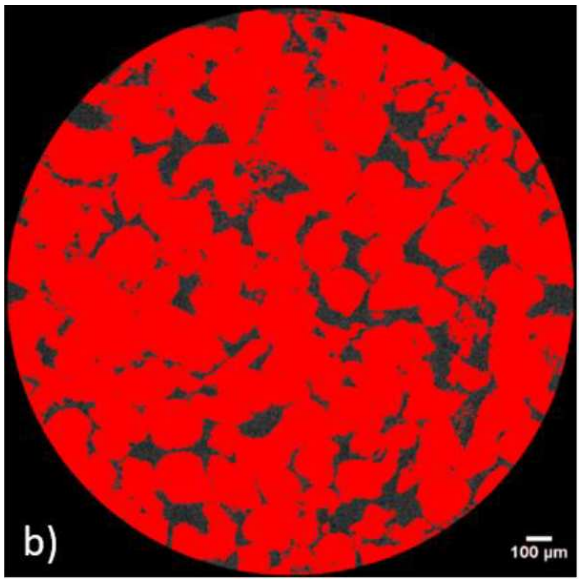

(b) Threshold image.

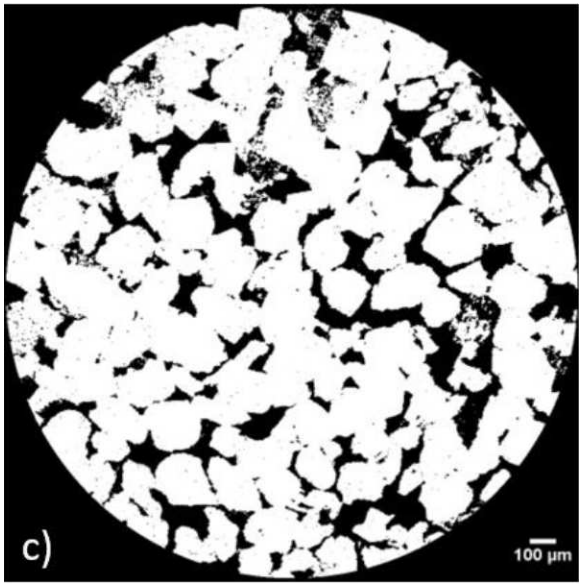

(c) Binarized image.

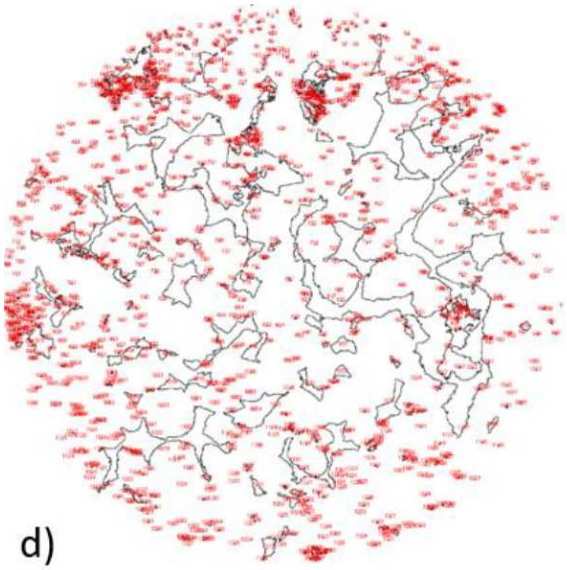

(d) Outline of pores in a binarized image.

Figure 2.11: Porosity and aspect ratio calculation from the μ-CT scan images.

CHAPTER 3

RESULTS

The main objective of this chapter is to summarize all the observation and measurements conducted by X-ray computed tomography, NMR, SIP, helium porosity (CMS-300) and ultrasonic measurements. Static pore volume compressibility was obtained from the measure of the change in pore volume caused by a change in applied stress (Zimmerman et al. 1986). Dynamic pore volume compressibility was determined using compressional and shear velocity measurements in different confining pressures to estimate the dry bulk modulus (K_{dry}).

3.1 X-ray computed tomography (μ-CT)

Micro X-Ray Computed Tomography (μ-CT) scans were acquired for four sandstone samples (Figure 3.1) that were used for NMR high pressure experiment. The scans acquired are composed of pixels with length of 2.25 μm. Due to this, pores less than 2.25 μm is not detectable by the device. From the observed scans, brighter colored elements can be seen. The brighter color represents higher density minerals, these minerals could possible be pyrite or chemically altered compounds. This is verified by the provided XRD data (Table 3.6). From the XRD data, we can determine that Berea, H1, and J1 samples contain pyrite minerals.

The pore size distribution obtained from the μ-CT scans for each sample provide information on the size of the pores (Figure 3.2). The pore size range between 2.25 - 165.8 μm, 2.25 - 215.7 μm, 2.25 - 149.2 μm, and 2.25 - 117.7 μm for Berea, H1, J1, and 23A sample respectively. The pore size measurements are also shown on the acquired μ-CT image scans (Figure 3.1). The higher pore size distribution observed from the μ-CT scans is due to the pores being accepted as cylinder.

As mentioned on the methodology chapter, 8 slices from the image sequence for each sample was chosen and processed using the ImageJ software. Using the ImageJ software average porosity of the sample, and the aspect ratio of the pores was determined (Table 3.1). The porosity values determined for these samples are 24 %, 21.5 %, 11.4 %, and 23.5 % for Berea, H1, J1, and 23A sample respectively. The pore aspect ratios are 0.3 for Berea, 0.6 for H1, 0.36 for J1, and 0.42 for 23A sample. Also, it must be mentioned that, the porosity and pore aspect ratio determined could be prone to error. This error is related with threshold value determined for the μ-CT images, which corresponds with the quality of the scan. The porosity values determined from the μ-CT image scans have between 3 – 10 % error compared with the porosity values determined using the CMS-300 helium porosity.

Table 3.1: Porosity and aspect ratio determined for Berea, H1, J1, and 23A samples from μ-CT scan.

Sample	**Porosity (%)**	**Aspect ratio**
Berea	23.89	0.327
H1	21.50	0.464
J1	11.42	0.547
23A	23.48	0.852

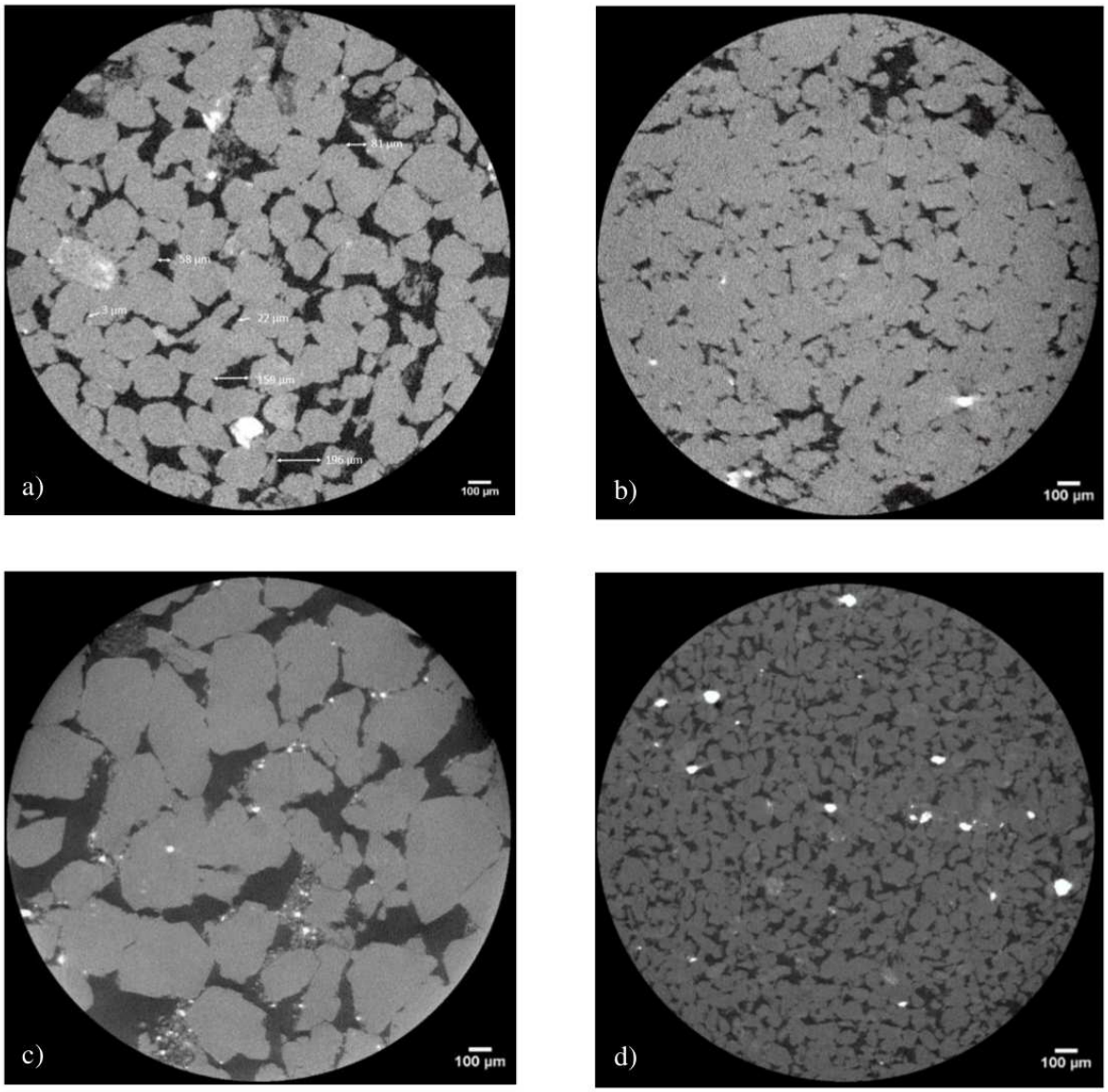

Figure 3.1: μ-CT images of a) Berea, b) J1, c) H1, c) 23A samples. Porosities determined from μ-CT images are: a) 23.89%, c) 11.416%, b) 21.5%, d) 23.482%.

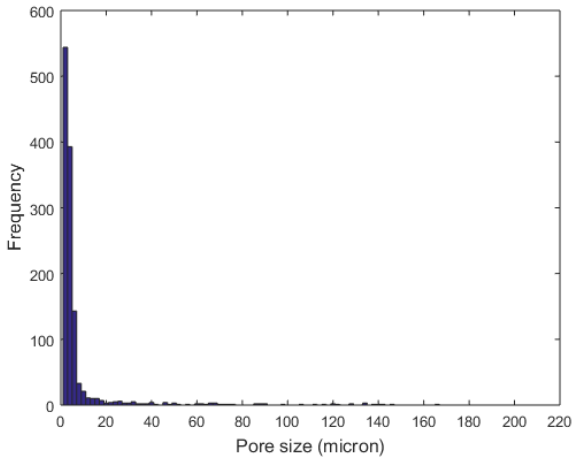

(a) Pore size distribution of Berea sample.

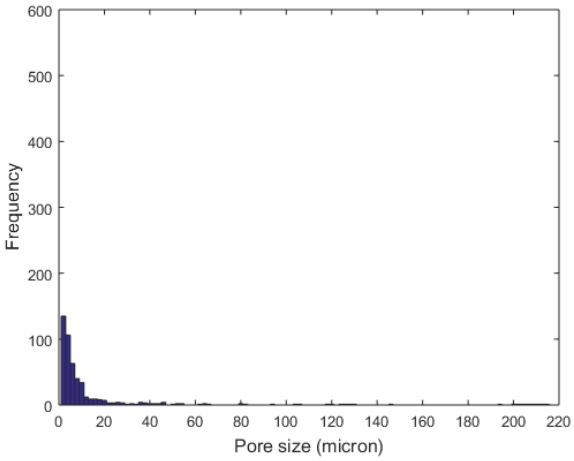

(b) Pore size distribution of H1 sample.

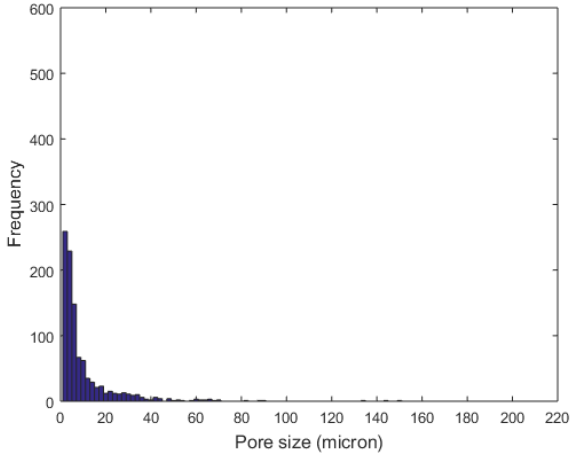

(c) Pore size distribution of J1 sample.

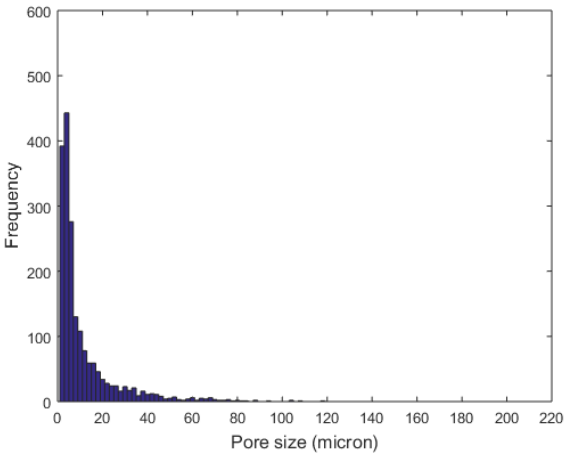

(d) Pore size distribution of 23A sample.

Figure 3.2: Histograms of pore size distributions for studied samples, derived from μ-CT images using image processing techniques.

3.2 Helium porosity and permeability

Helium porosity and permeability measurements were conducted for 11 samples. 10 Hibernia oil field samples were pressurized up to maximum confining pressure of 10 MPa, while Berea sample was conducted up to 17 MPa confining pressure. The data was acquired at 3.5 MPa pressure intervals. Table 3.2 and Table 3.3 illustrates the pressure dependency of porosity and permeability for the given 11 samples. Porosity and permeability decrease as a function of pressure can be observed. The measured porosity values match with the data provided by Dr. Manika Prasad (Table 3.4).

The water immersion porosimetry (WIP) was conducted for four samples (Berea, H1, J1, and 23A) pre - and post helium porosity and permeability measurements (Table 3.5). The purpose of this measurements

were to determine the porosity at atmospheric condition, as helium porosity and permeability measurements can not be conducted below 3.5 MPa confining pressure. The WIP porosity at atmospheric condition and the helium porosity at elevated pressure were used to correlate the NMR high pressure data.

The relationship between the measured helium porosity (CMS-300), porosity provided by the courtesy of Manika Prasad, and the NMR porosity calculated at ambient pressure can be observed in Figure 3.3. From the relationship, good correlation between the three porosity values can be seen.

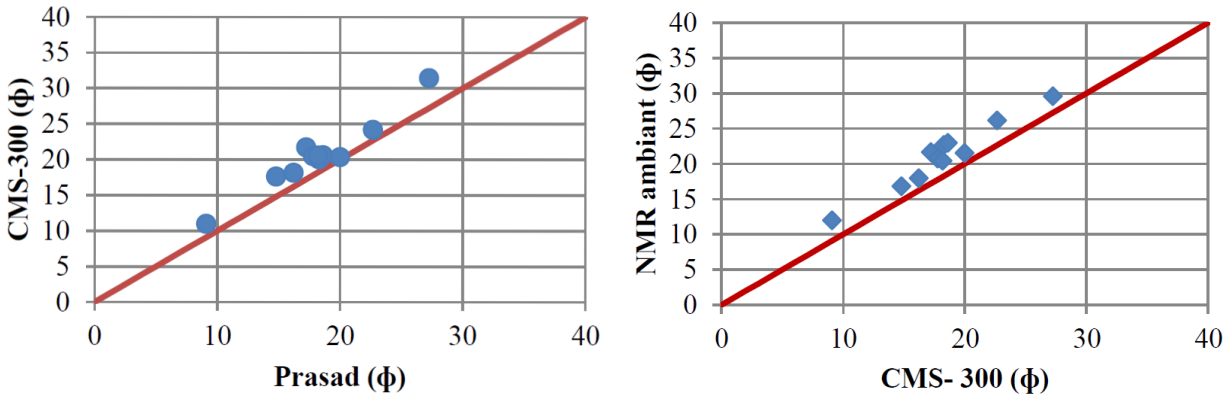

(a) (b)

Figure 3.3: Relationship between different porosity measurements. (a) Correlation between helium porosity and porosity provided by the courtesy of Manika Prasad. (b) Correlation between NMR porosity and helium porosity.

3.3 XRD measurements

Ternary diagram (Figure 3.4) and mineralogical summary by percentile (Table 3.6), which was provided by courtesy of Manika Prasad, present X-ray powder diffraction (XRD) measurements for 10 Hibernia and 6 Ben-Nevis samples. The samples mostly consist of quartz mineralogy ranging between 79 - 99 %. Other mineralogical constitution of the samples are K-Feldspar, plagioclases, dolomite, calcite, pyrite, and clay.

3.4 Ultrasonic measurements

Ultrasonic compressional (P) and shear (S) wave velocities depending on the pressure are shown through Figure 3.5 to Figure 3.15. Velocities of each pressure step is summarized in Table 3.7 to Table 3.9. The Figure 3.5 to Figure 3.12 and the pressure summarization of Table 3.9 represents the ultrasonic measurements for provided Hibernia oil field formation samples (Courtesy of Manika Prasad). Figure 3.14 and Table 3.7 provides the data acquired for Berea sample under dry condition with velocity orientation of 0, 45, and 90 degrees. The Figure 3.15 and Table 3.8 provides the acquired data for Berea sample under saturated condition with same orientation as the dry measurements. The ultrasonic measurements, during the pressurization

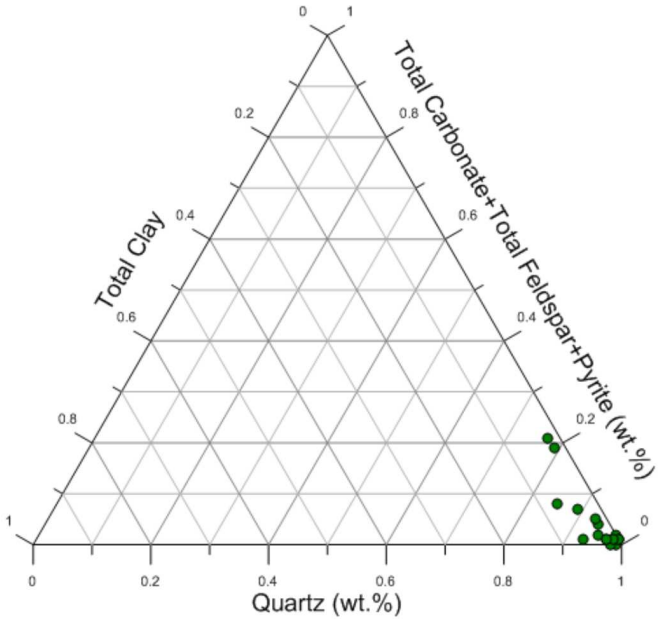

Figure 3.4: Ternary diagram for samples.

exhibits large increase during the initial microcrack closure stage, and finally reaching an asymptotic value at higher pressure which corresponds with the stiffness of the sample.

Figure 3.13 presents the compressional and shear wave velocities for all Hibernia and Ben-Nevis reservoir samples. From Figure 3.13 , high compressional and shear wave velocities can be detected for Hibernia reservoir samples compared to Ben-Nevis. Hibernia samples have compressional wave velocity of 4 km/s and higher, and shear wave velocity of higher than 2.5 km/s at the confining pressure of 60 MPa. Compared to Hibernia reservoir samples Ben-Nevis samples have compressional wave velocity between 3 - 4 km/s and shear wave velocity ranging between 2 - 2.4 km/s at the same confining pressure of 60 MPa. The lower velocity values for Ben-Nevis samples is due to the high clay content and porosity of the samples. The Hibernia samples have lower porosity compared to Ben-Nevis, porosity value for Hibernia samples are below 21 %, while Ben-Nevis samples have porosity value higher than 24 %. Also, Hibernia samples are homogeneous, mainly composed of quartz mineral, while Ben-Nevis consists of variety of mineralogy.

3.5 Nuclear magnetic resonance (NMR)

Figure 3.16 to Figure 3.22 provides the T_2 distribution for 13 samples under ambient condition, and Figure 3.23 to Figure 3.26 shows T_2 distribution converted to size domain for four samples (Berea, H1, J1, 23A) under confining pressure up to 10 MPa with 3.5 MPa pressure steps. Figure 3.26, which represents the 23A sample had failure at 10 MPa and due to this data up to 7 MPa can be observed. Pore size distribution for Hibernia samples (H1, J1, and 23A) and Berea sample were obtained from NMR T_2 distribution by

converting the time domain to size domain using relaxivity value obtained from literature (Marschall et al. 1995) and adjusted to the samples using the XRD minerology (Table 3.6). The surface relaxivity values used on these samples are as follows: 21.03 μm/s - Berea, 22.95 μm/s - H1, 22.6 μm/s - J1, and 21.32 μm/s - 23A sample. Pore size distribution from NMR measurement for pressurization and depressurization is depicted from Figure 3.23 to Figure 3.26, a) being the pressurization procedure of conducted experiment and b) depressurization process.

From the T_2 distribution, bimodal and rarely unimodal distribution is demonstrated for the formation. Peak incremental porosity represents the dominant pore size ranges. The porosity for each sample was calculated from the NMR T_2 distribution. As mentioned in the previous section, the NMR has good correlation with the porosity acquired from helium porosity and the porosity data provided by Manika Prasad (Figure 3.3).

3.6 SIP measurements

Figure 3.27 presents the raw data used to calculate the SIP pore size distribution. Figure 3.28 demonstrates the SIP pore size distribution for pressurization and de-pressurization stages. The experiment was performed up to maximum confining pressure of 17 MPa. This data was used to calculate the pore compressibility from the pore size distribution. The figure shows a bimodal pore-size distribution. Decrease in incremental porosity corresponds with the increase of confining pressure. The SIP pore size distribution shows two pore clusters. Pores ranging between 0.2 – 2 micrometers, and 4 – 13 micrometers. The pores less than 0.2 micrometer are not detected; this is due to the resolution of the apparatus. The shift to the right on x axis (pore size) for pores ranging between 0.2 – 2 micrometers is linked with the compression of pores ranging between 4 - 13 micron.

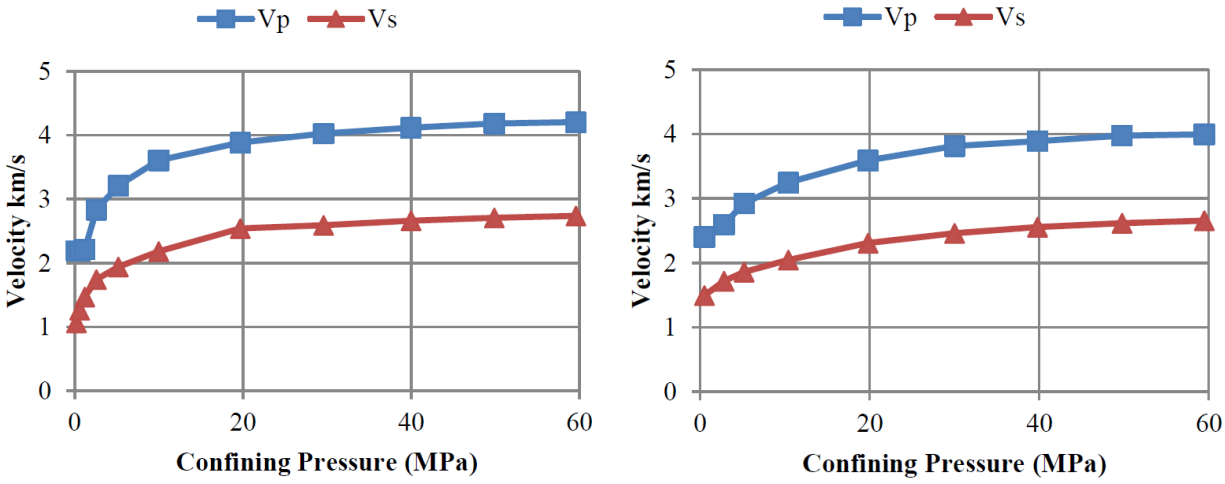

(a) (b)

Figure 3.5: Compressional and shear velocity fit for samples (a) A1 and (b) B1

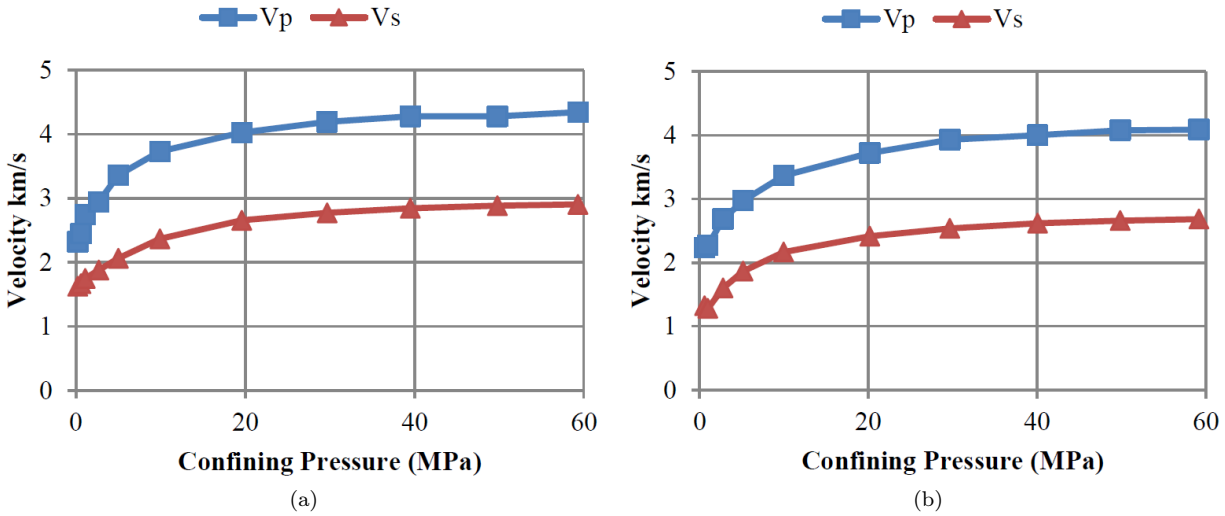

(a) (b)

Figure 3.6: Compressional and shear velocity fit for samples (a) C1 and (b) D1

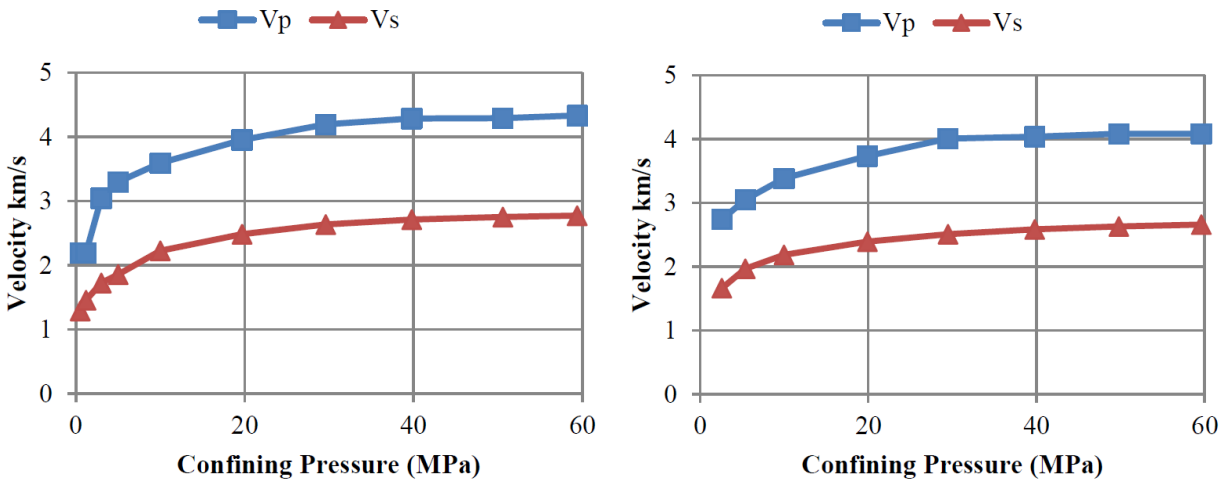

Figure 3.7: Compressional and shear velocity fit for samples (a) G1 and (b) H1

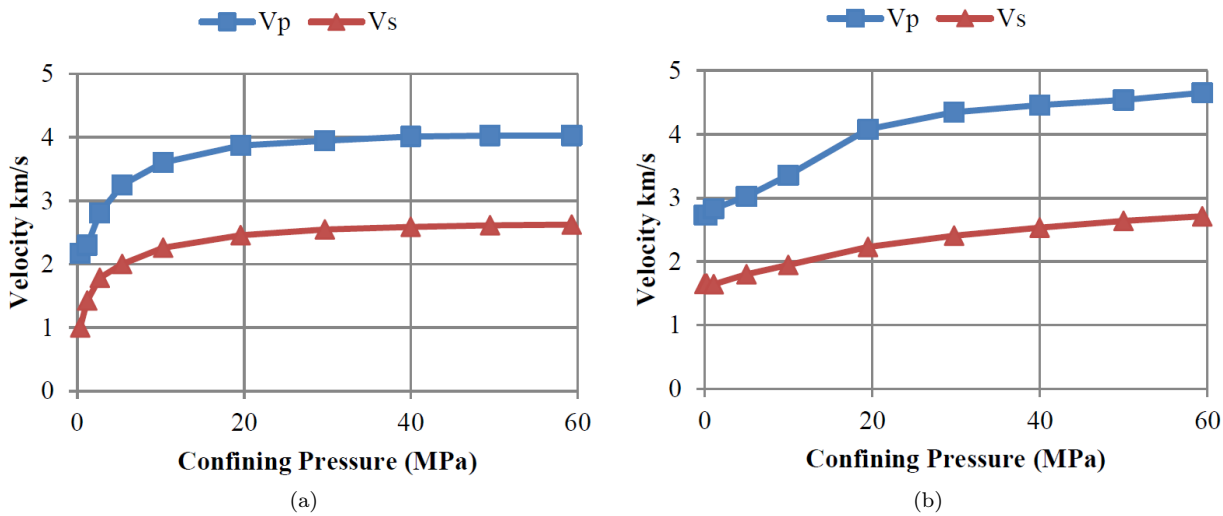

Figure 3.8: Compressional and shear velocity fit for samples (a) M1 and (b) J1

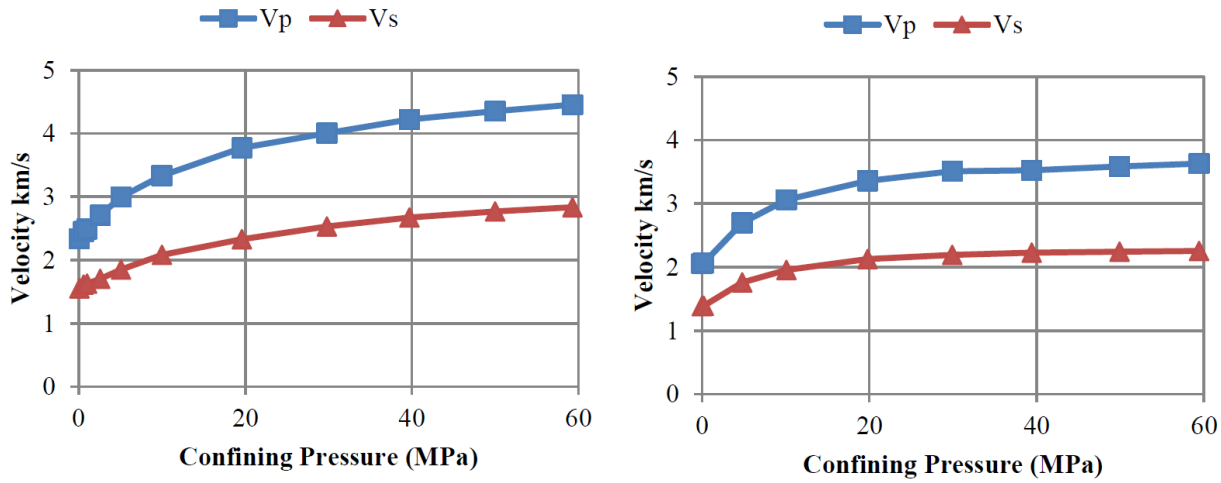

(a) (b)

Figure 3.9: Compressional and shear velocity fit for samples (a) J2 and (b) 23A

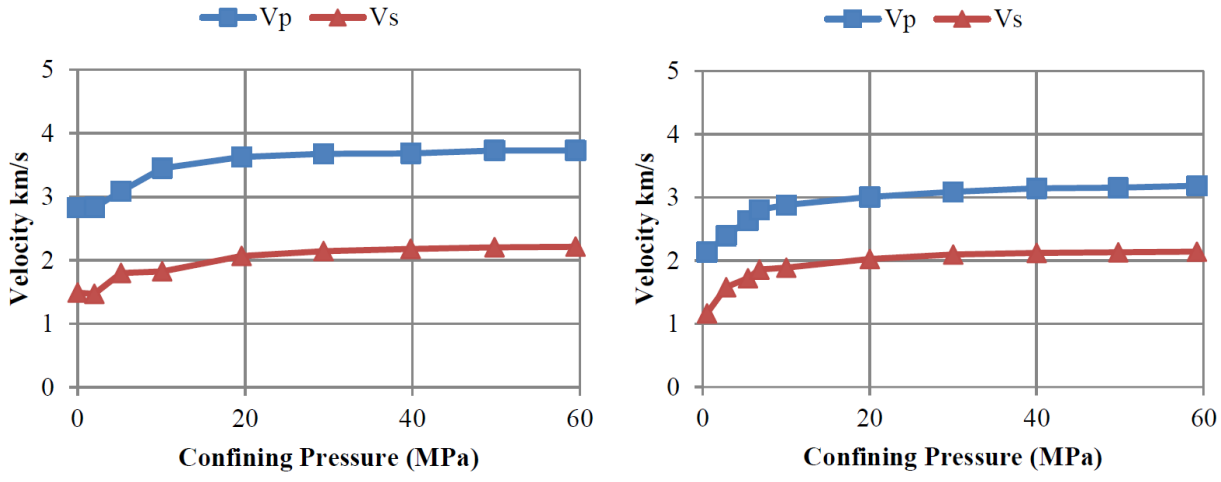

(a) (b)

Figure 3.10: Compressional and shear velocity fit for samples (a) 26A and (b) 65A

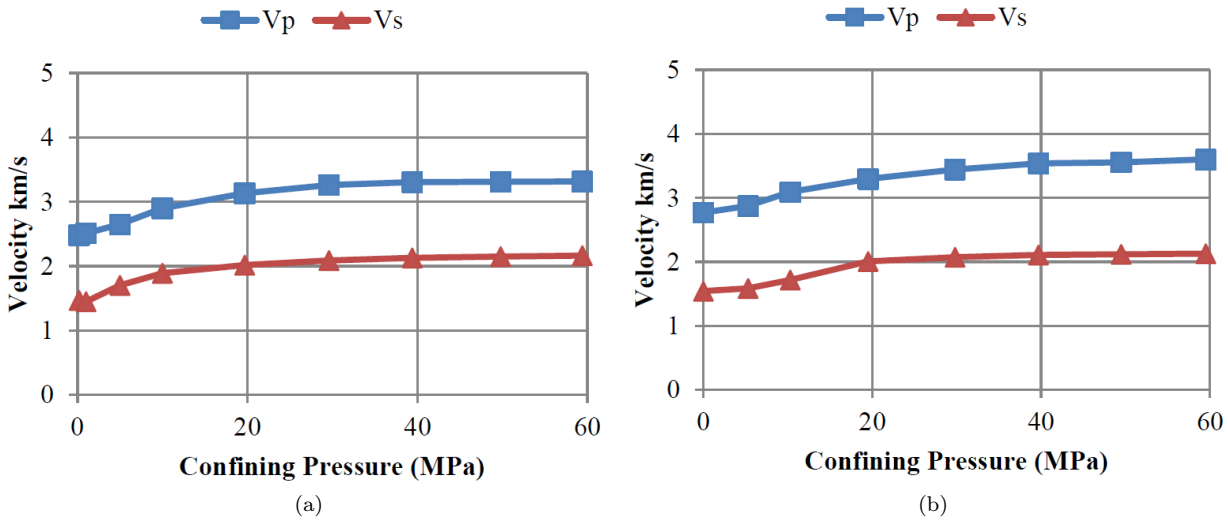

Figure 3.11: Compressional and shear velocity fit for samples (a) 71A and (b) 92A

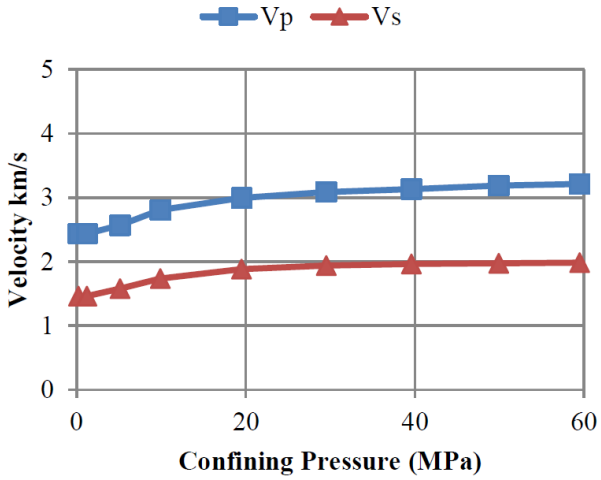

Figure 3.12: Compressional and shear velocity fit for sample 99A

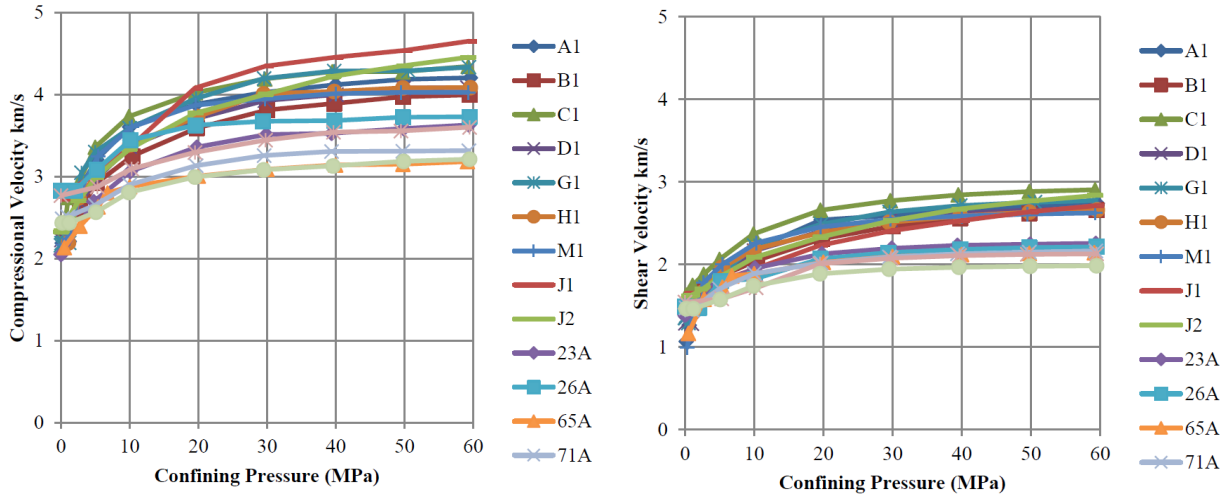

(a) (b)

Figure 3.13: Ultrasonic velocity measurements for all Hibernia and Ben-Nevis samples. Hibernia reservoir samples have higher compressional and shear velocities compared to Ben-Nevis reservoir samples. (a) Compressional wave velocity. (b) Shear wave velocity.

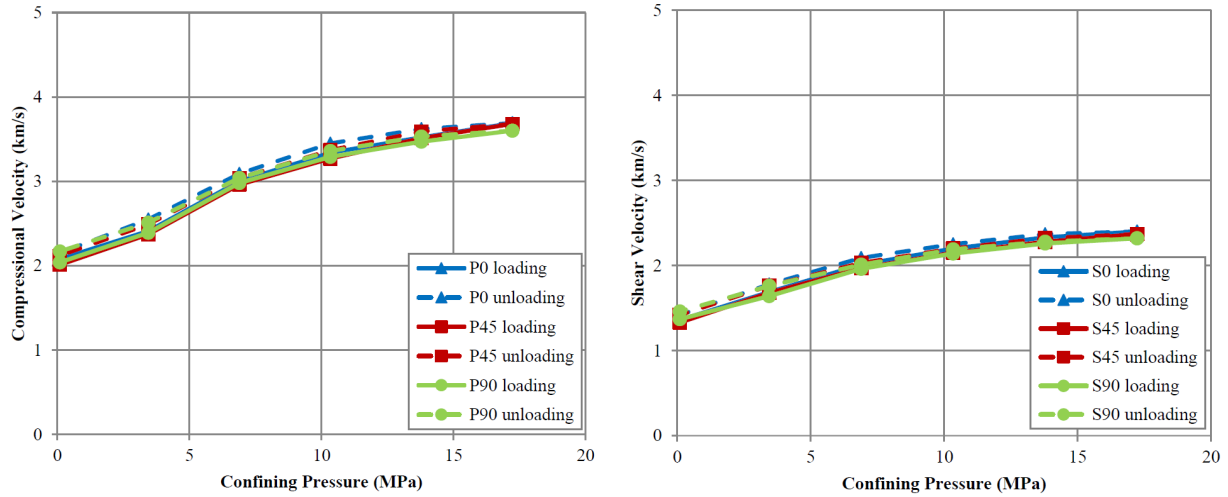

(a) (b)

Figure 3.14: Dry ultrasonic velocity measurements for Berea sample at orientation of 0, 45, and 90 degrees, isotropy of the sample can be observed. (a) Compressional wave velocity. (b) Shear wave velocity.

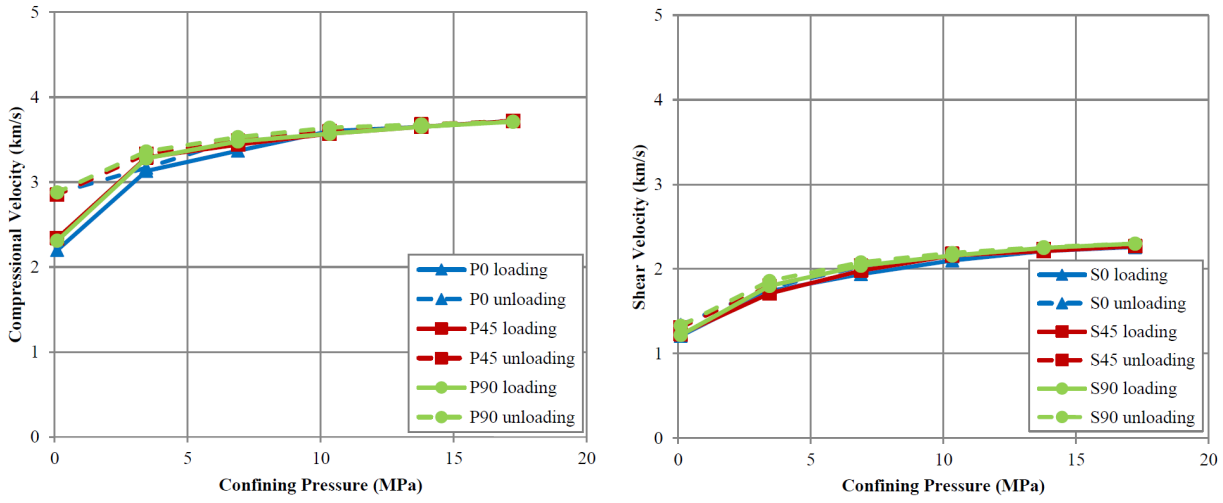

(a) (b)

Figure 3.15: Saturated ultrasonic velocity measurements for Berea sample at orientation of 0, 45, and 90 degrees, isotropy of the sample can be observed. (a) Compressional wave velocity. (b) Shear wave velocity.

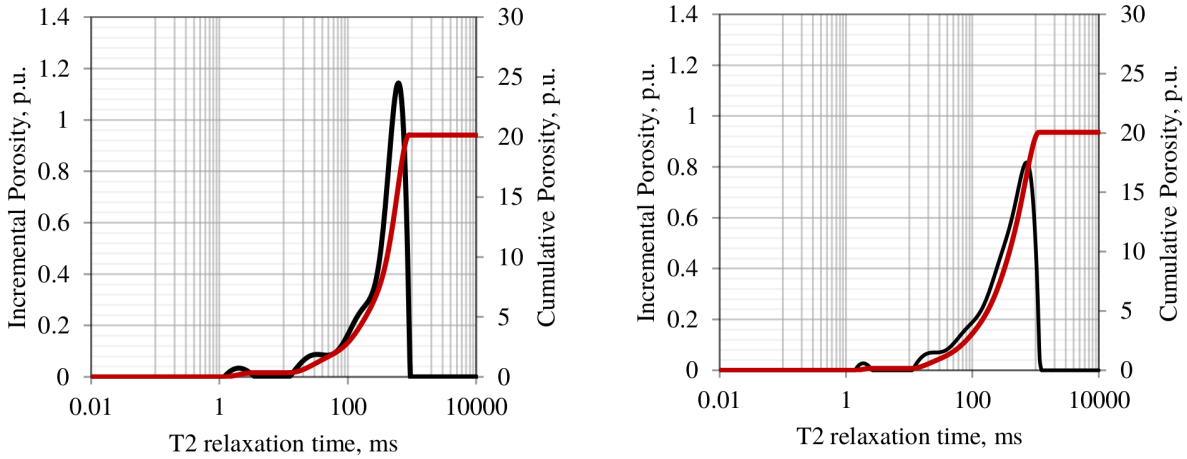

(a) (b)

Figure 3.16: Pore size distribution and cumulative porosity for samples (a) A1 and (b) B1

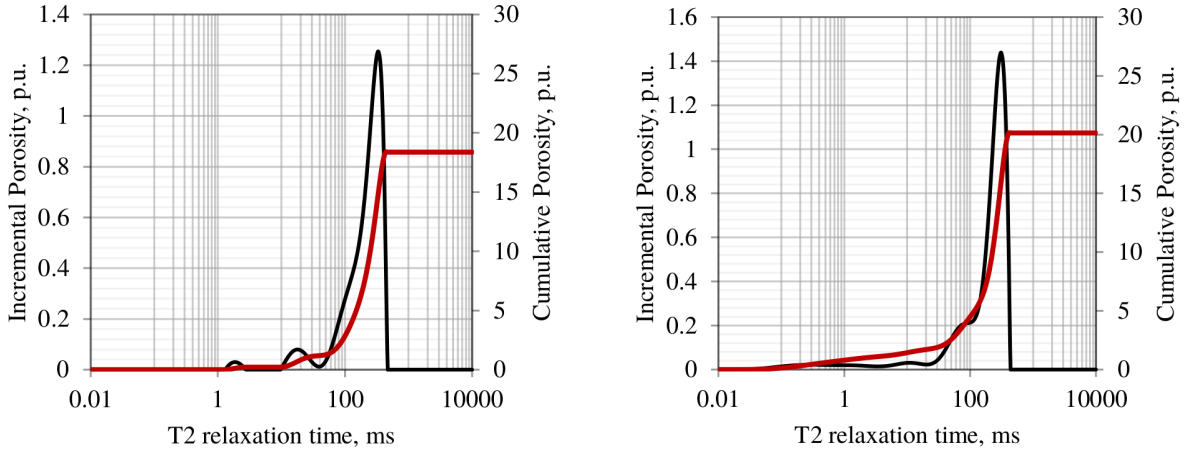

Figure 3.17: Pore size distribution and cumulative porosity for samples (a) C1 and (b) D1

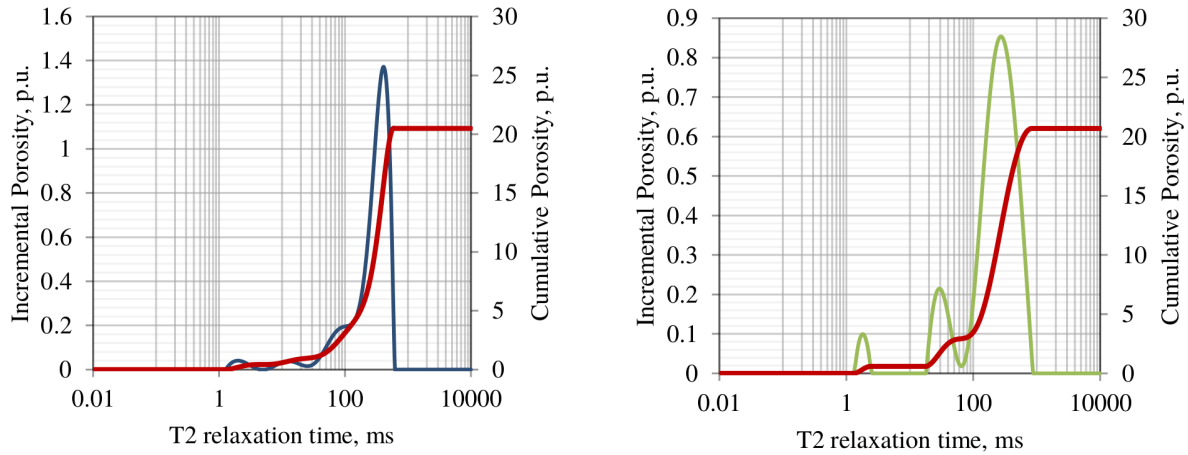

Figure 3.18: Pore size distribution and cumulative porosity for samples (a) G1 and (b) H1

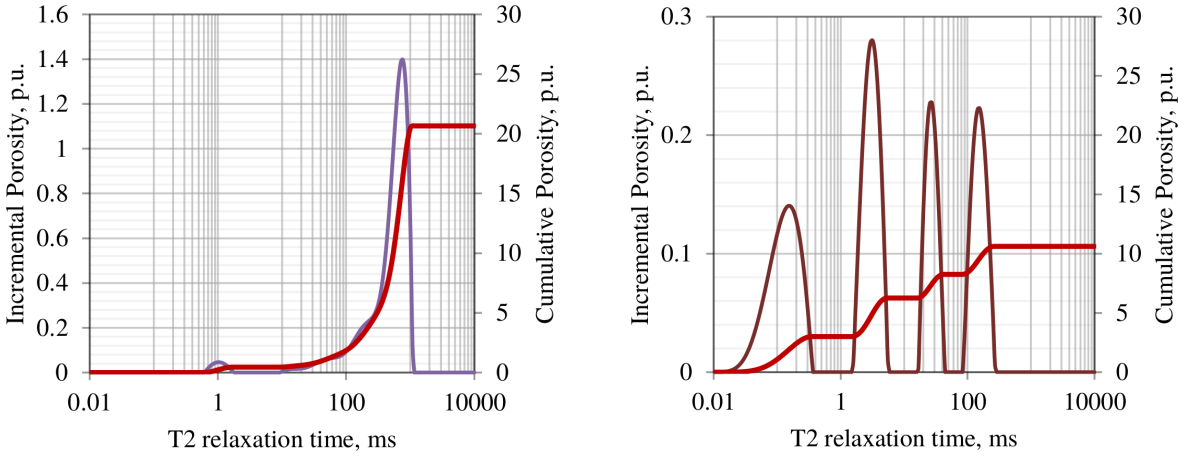

(a) (b)

Figure 3.19: Pore size distribution and cumulative porosity for samples (a) M1 and (b) J1

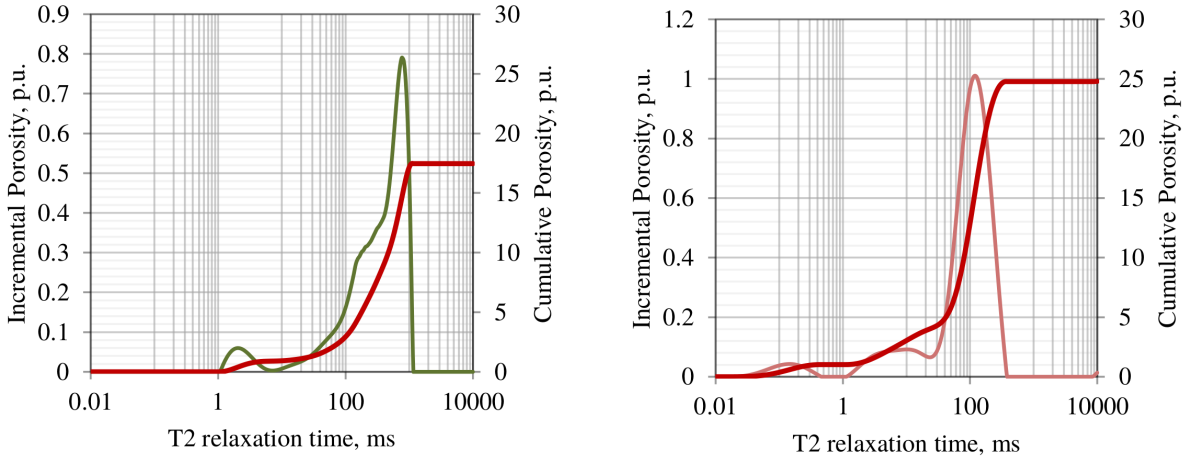

(a) (b)

Figure 3.20: Pore size distribution and cumulative porosity for samples (a) J2 and (b) 23A

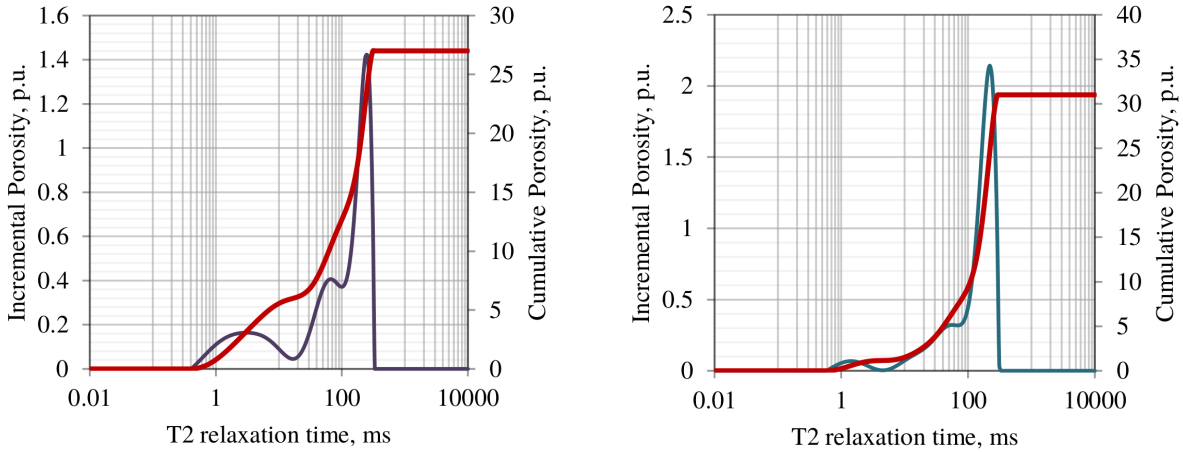

Figure 3.21: Pore size distribution and cumulative porosity for samples (a) 26A and (b) 71A

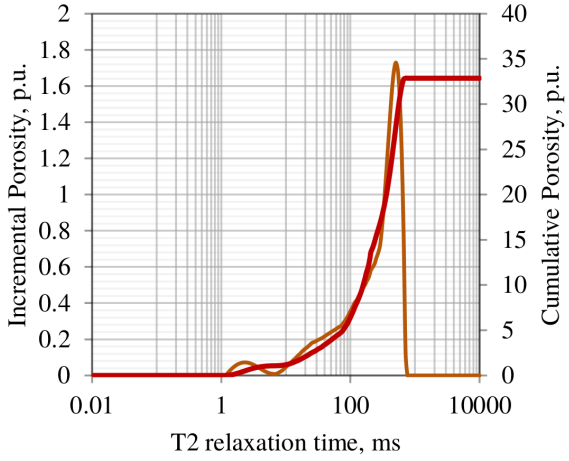

Figure 3.22: Pore size distribution and cumulative porosity for sample 92A

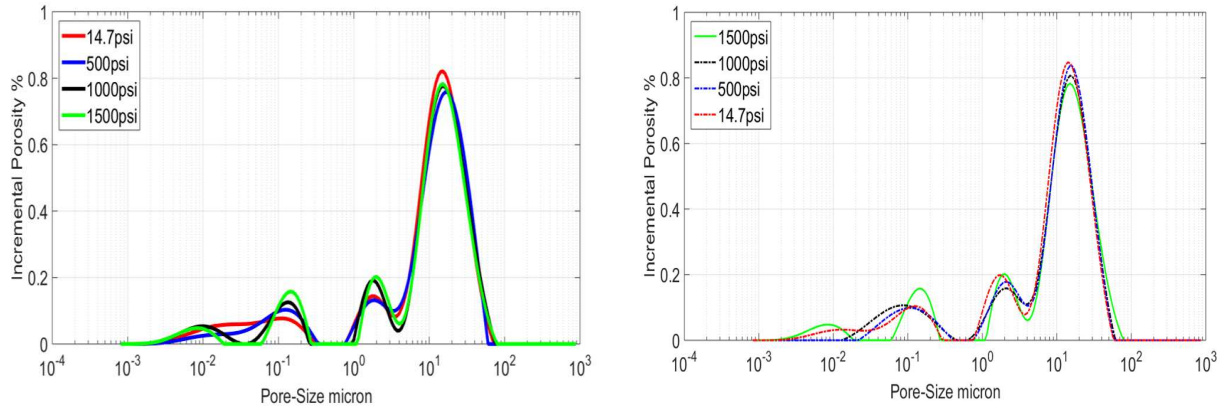

(a) (b)

Figure 3.23: NMR high pressure pore-size distribution for Berea sample using surface relaxivity value of 21.03 μm/s. (a) Loading confining pressure. (b) Unloading confining pressure.

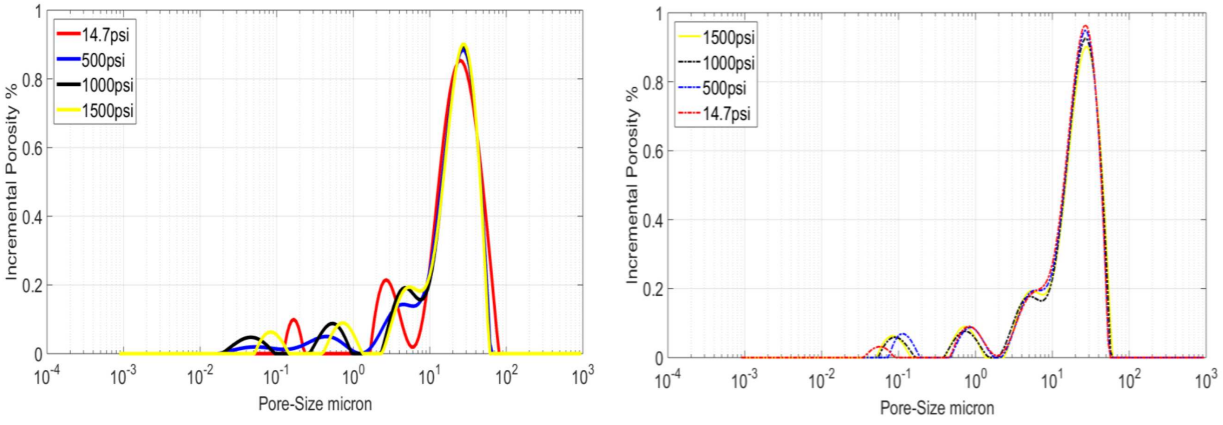

(a) (b)

Figure 3.24: NMR high pressure pore-size distribution for H1 sample using surface relaxivity value of 22.95 μm/s. (a) Loading confining pressure. (b) Unloading confining pressure.

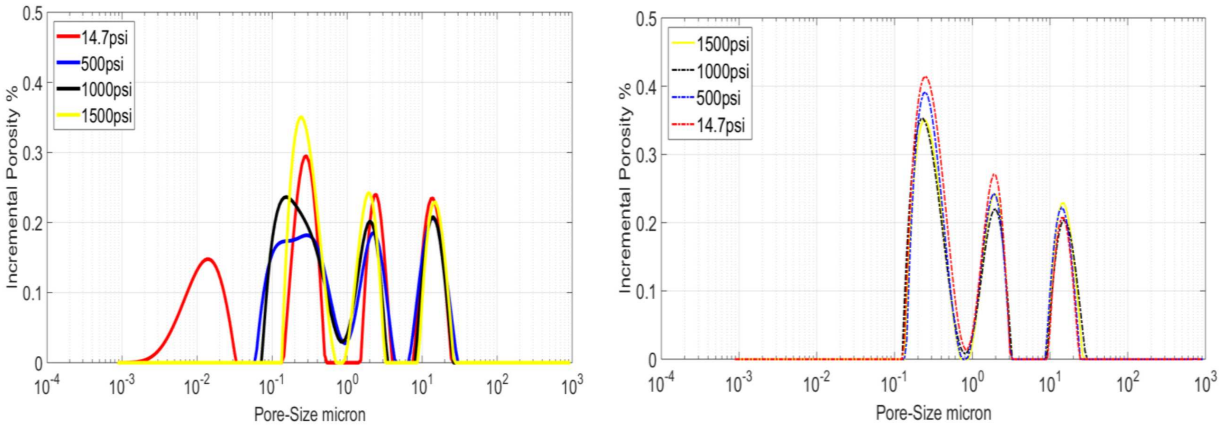

(a) (b)

Figure 3.25: NMR high pressure pore-size distribution for J1 sample using surface relaxivity value of 22.6 μm/s. (a) Loading confining pressure. (b) Unloading confining pressure.

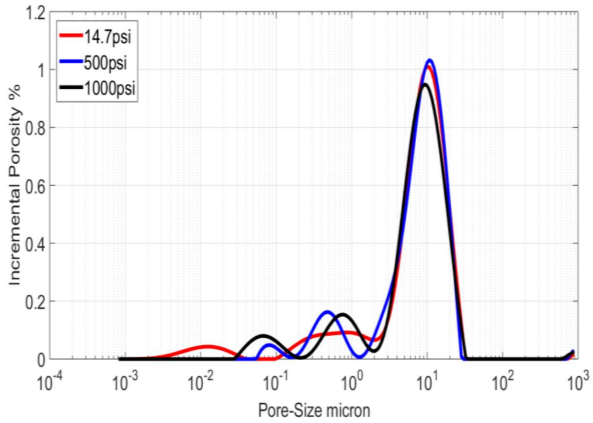

Figure 3.26: NMR high pressure pore-size distribution for 23A sample using surface relaxivity value of 21.32 μm/s. Figure depicts the loading up to 7 MPa. The experiment could not be continued due to failure at 10 MPa.

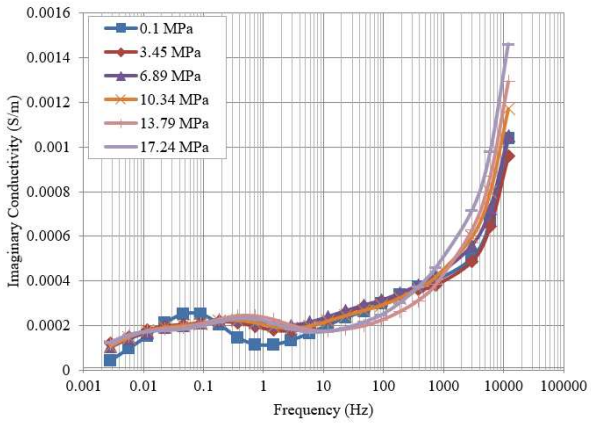

Figure 3.27: Imaginary conductivity measurements used for calculating the SIP pore-size distribution.

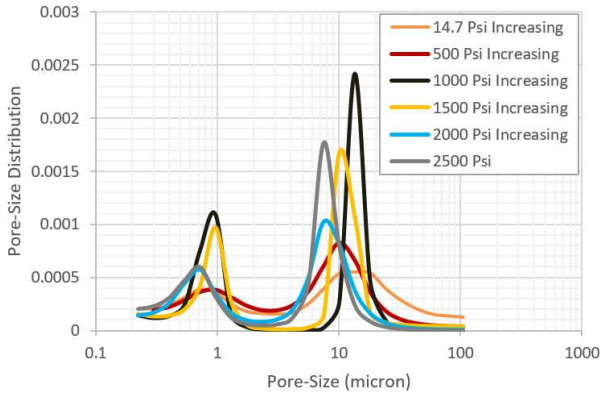

Figure 3.28: Berea pore-size distribution from SIP under increasing confining pressure.

Table 3.2: Helium permeability measured at different pressure conditions.

		Confining pressure (MPa)								
		3.45	6.89	10.34	13.79	17.24	13.79	10.34	6.89	3.45
Permeability (mD)	Berea	1050	1020	1012	997	987	996	1010	1016	1040
	J1	2.64	2.49	2.37	2.29			2.36	2.46	2.62
	H1	3690	3667	3610	3582			3606	2655	3680
	23A	277	271	266	263			265	270	275
	A1	6560	6210	6105	6050					
	C1	2110	2080	2070	2050					
	D1	1320	1260	1230	1224					
	M1	4610	4390	4290	4120					
	G1	2040	2010	1990	1970					
	26A	186	183	182.5	182					
	71A	1670	1630	1580	1570					

Table 3.3: Helium porosity measured at different pressure conditions.

		Confining pressure (MPa)								
		3.45	6.89	10.34	13.79	17.24	13.79	10.34	6.89	3.45
Porosity (%)	Berea	23.12	22.83	22.67	22.55	22.4	22.5	22.61	22.78	23.03
	J1	10.37	10.175	10	9.91			9.95	10.02	10.095
	H1	20.06	19.985	19.9	19.83			19.88	19.92	19.994
	23A	24.2	24.01	23.93	23.79			23.88	23.96	24.15
	A1	19.53	18.87	18.63	18.43					
	C1	17.67	17.41	17.29	17.22					
	D1	19.06	18.79	18.64	18.55					
	M1	19.94	19.48	19.25	19.14					
	G1	19.68	19.38	19.25	19.16					
	26A	20.57	20.31	20.17	20.08					
	71A	28.92	28.27	27.92	27.71					

Table 3.4: Porosity measurements provided by Dr. Manika Prasad up to confining pressures of 60 MPa.

	Confining pressure (MPa)						
	5	10	20	30	40	50	60
A1	21.68	21.61	21.54	21.48	21.43	21.39	21.35
B1	21.34	20.58	21.00	21.08	21.00	20.93	20.87
C1	18.15	18.1	18.04	18.00	17.96	17.92	17.89
D1	20.46	20.4	20.33	20.29	20.25	20.21	20.18
G1	20.58	20.52	20.43	20.38	20.33	20.29	20.26
H1	20.02	19.94	19.85	19.8	19.74	19.70	19.66
J1	10.96	10.81	10.68	10.61	10.56	10.52	10.49
J2	17.59	17.51	17.43	17.37	17.32	17.29	17.26
M1	20.62	20.58	20.38	20.33	20.29	20.25	20.22
23A	24.14	24.13	24.00	23.88	23.84	23.77	23.71
26A	20.35	20.21	20.09	19.99	19.94	19.89	19.84
65A	30.67	30.56	30.56	30.47	30.67	30.73	30.67
71A	30.36	30.2	30.02	29.91	29.8	29.72	29.64
92A	31.42	31.23	31.55	31.39	31.26	31.13	31.03
99A	33.60	33.44	33.24	33.09	32.95	32.83	32.72

Table 3.5: Porosity measured before and after helium porosity using WIP (Water immersion porosimetry).

	WIP porosity (%)			
	Berea	J1	H1	23A
Before loading	24.11	10.65	20.32	24.8
After loading	23.85	10.27	20.17	24.62

Table 3.6: XRD mineralogy results by weight percentage.

Formation	Sample ID	**Whole rock mineralogy (wt %)**						
		Quartz	K-feldspar	Plagioclase	Calcite	Dolomite	Pyrite	Total clay
Hibernia	A1	99	0	0	0	0	0	1
	B1	93	0	0	0	0	1	6
	F1	98	0	0	0	0	2	0
	H1	99	0	0	0	0	1	0
	M1	99	0	0	0	0	1	0
	C1	98	0	0	0	0	0	2
	D1	97	0	0	0	0	1	2
	G1	98	0	0	0	0	1	1
	J1	95	0	1	0	0	1	3
	J2	97	0	1	0	0	0	2
Ben-Nevis	23A	85	3	4	1	0	0	7
	26A	89	2	3	1	0	1	4
	65A	94	1	1	1	0	1	2
	71A	93	1	1	2	0	1	2
	92A	77	2	3	15	0	1	2
	99A	79	2	3	12	1	1	2

Table 3.7: Results for dry compressional and shear wave velocities in 0, 45, 90 degrees orientation under pre-and post-confining pressure for Berea sample, with maximum confining pressure of 17.24 MPa.

Confining pressure (MPa)	**Ultrasonic velocity (km/s)**					
	V_p^0	V_p^{45}	V_p^{90}	V_s^0	V_s^{45}	V_s^{90}
0.10	2.08	2.01	2.04	1.36	1.33	1.37
3.45	2.41	2.37	2.39	1.69	1.68	1.64
6.89	3	2.96	2.98	2.01	1.97	1.96
10.34	3.34	3.27	3.29	2.2	2.15	2.14
13.79	3.52	3.51	3.47	2.33	2.28	2.26
17.24	3.69	3.68	3.6	2.4	2.37	2.32
13.79	3.62	3.59	3.53	2.37	2.32	2.28
10.34	3.45	3.37	3.36	2.25	2.2	2.19
6.89	3.09	3.04	3.04	2.09	2.03	2.01
3.45	2.55	2.49	2.51	1.78	1.76	1.76
0.10	2.15	2.12	2.17	1.42	1.42	1.46

Table 3.8: Results for saturated compressional and shear wave velocities in 0, 45, 90 degrees orientation under pre-and post-confining pressure for Berea sample, with maximum confining pressure of 17.24 MPa.

Confining pressure (MPa)	**Ultrasonic velocity (km/s)**					
	V_p^0	V_p^{45}	V_p^{90}	V_s^0	V_s^{45}	V_s^{90}
0.10	2.2	2.34	2.31	1.21	1.23	1.22
3.45	3.13	3.29	3.28	1.74	1.71	1.8
6.89	3.37	3.44	3.48	2.84	1.98	2.04
10.34	3.6	3.57	3.57	2.1	2.16	2.16
13.79	3.65	3.65	3.65	2.21	2.21	2.25
17.24	3.72	3.72	3.71	2.26	2.27	2.3
13.79	3.67	3.68	3.68	2.23	2.24	2.26
10.34	3.62	3.6	3.64	2.15	2.18	2.19
6.89	3.51	3.49	3.53	2.03	2.04	2.08
3.45	3.17	3.33	3.36	1.78	1.8	1.86
0.10	2.87	2.85	2.88	1.34	1.31	1.33

Table 3.9: Ultrasonic velocity (km/s) measurements under confining pressure (MPa) conditions (Courtesy of Manika Prasad).

		Confining pressure (MPa)						
		0.1	10	20	30	40	50	60
A1	Vp	2.195	3.611	3.889	4.034	4.119	4.186	4.206
	Vs	1.051	2.189	2.547	2.599	2.673	2.712	2.741
B1	Vp	2.357	3.225	3.592	3.806	3.904	3.973	3.995
	Vs	1.438	2.023	2.303	2.459	2.561	2.619	2.655
C1	Vp	2.306	3.737	4.035	4.194	4.281	4.277	4.35
	Vs	1.609	2.373	2.654	2.776	2.849	2.889	2.908
D1	Vp	2.204	3.354	3.71	3.932	4.01	4.088	4.088
	Vs	1.224	2.17	2.417	2.53	2.612	2.664	2.682
G1	Vp	2.106	3.585	3.961	4.191	4.275	4.29	4.339
	Vs	1.214	2.217	2.493	2.635	2.711	2.745	2.771
H1	Vp	2.483	3.38	3.737	4.014	4.044	4.083	4.092
	Vs	1.495	2.182	2.396	2.516	2.588	2.639	2.657
J1	Vp	2.695	3.338	4.082	4.34	4.443	4.519	4.637
	Vs	1.618	1.937	2.233	2.394	2.516	2.631	2.695
J2	Vp	2.319	3.327	3.785	4.011	4.227	4.354	4.442
	Vs	1.54	2.079	2.327	2.532	2.67	2.757	2.813
M1	Vp	2.137	3.591	3.874	3.944	4.004	4.031	4.027
	Vs	0.935	2.253	2.453	2.536	2.583	2.609	2.619
23A	Vp	2.048	3.047	3.37	3.512	3.529	3.588	3.624
	Vs	1.382	1.953	2.131	2.2	2.226	2.246	2.25
26A	Vp	2.832	3.441	3.631	3.677	3.687	3.727	3.728
	Vs	1.497	1.831	2.07	2.151	2.184	2.206	2.21
65A	Vp	2.099	2.885	3.018	3.097	3.154	3.162	3.191
	Vs	1.107	1.895	2.026	2.099	2.126	2.139	2.149
71A	Vp	2.487	2.904	3.143	3.267	3.315	3.312	3.319
	Vs	1.423	1.885	2.02	2.094	2.131	2.157	2.162
92A	Vp	2.771	3.084	3.305	3.45	3.532	3.554	3.596
	Vs	1.539	1.711	2.015	2.082	2.112	2.12	2.129
99A	Vp	2.439	2.812	3.001	3.093	3.138	3.19	3.215
	Vs	1.463	1.744	1.893	1.947	1.969	1.976	1.987

CHAPTER 4
DISCUSSION

Pore compressibility measurements of hydrocarbon reservoirs or in our case the rock samples are determined using uniaxial and triaxial measurement tools which is known as direct measurement method. However, most common approach of determining pore compressibility is indirect method using porosity, permeability, acoustic or sonic log data. The approach in this thesis is to determine pore compressibility from NMR perspective, which allows to determine not only total compressibility of the pore structure, but also each separate pore clusters by determination of pore size and porosity related to that pore sizes. The static pore compressibility was also determined from SIP and helium porosity (CMS-300) to verify the accuracy of the NMR pore compressibility, and static and dynamic pore compressibility correlation was developed by calculating the dynamic pore compressibility from acoustic measurement.

4.1 Pore size distribution

NMR measurement below ten milliseconds is negligible due to the ringing effect caused by the limitation of the device (Saidian 2015). 10 milliseconds converted to size domain is between 0.81-0.94 micrometers depending on the sample. The difference in these value is related to the surface relaxivity value used to convert the time into size domain. Accepting that the data below 10 milliseconds is negligible, bimodal distribution for Berea, H1, and J1 samples, and unimodal distribution for 23A sample can be depicted from the measurements (Figure 4.1 - Figure 4.4). Decrease in NMR signal amplitude and relaxation time for larger pore sizes is seen with increasing confining pressure for Berea, H1, and 23A samples. This corresponds with the increase in NMR signal amplitude and relaxation time for smaller pores for Berea and H1 sample. This effect is not seen for 23A sample due to bimodal pore distribution of this sample. The increase in amplitude and relaxation time of smaller pores for Berea and H1 sample is due to the increase in number of smaller pores during the compression of larger pores.

However, for J1 sample opposite effect can be observed (Figure 4.4). Increase in NMR signal amplitude and relaxation time for larger pore sizes and decrease NMR signal amplitude and relaxation time for smaller pores can be observed for J1 sample. This could be related to the crushing of the smaller pores, which could result in new pore structures with larger pore sizes.

As mention on the previous chapter SIP measurements (Figure 3.28) were performed on virgin Berea sample with maximum confining pressure of 17 MPa to compare the accuracy of acquired NMR data, and determine the correctness of the surface relaxivity value from mineralogy. Pore size distribution for both SIP

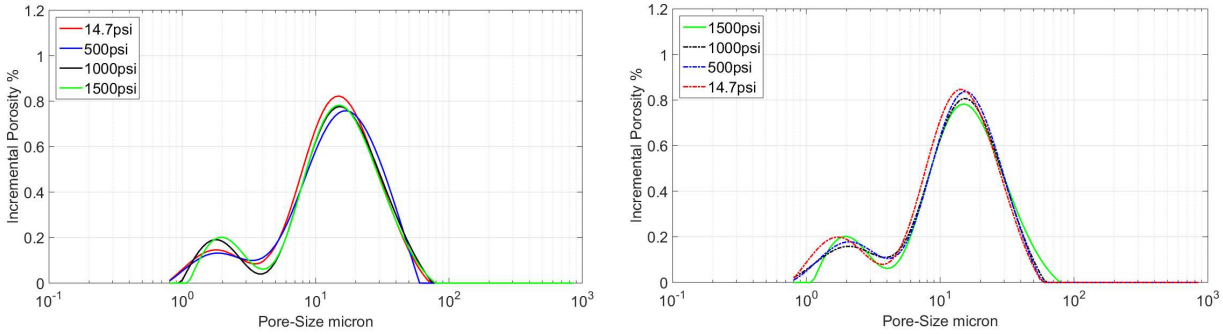

(a) (b)

Figure 4.1: NMR high pressure pore-size distribution for Berea sample. Data below 10 milliseconds is negligible due to the ringing effect caused by the limitation of the device. (a) Loading confining pressure. (b) Unloading confining pressure.

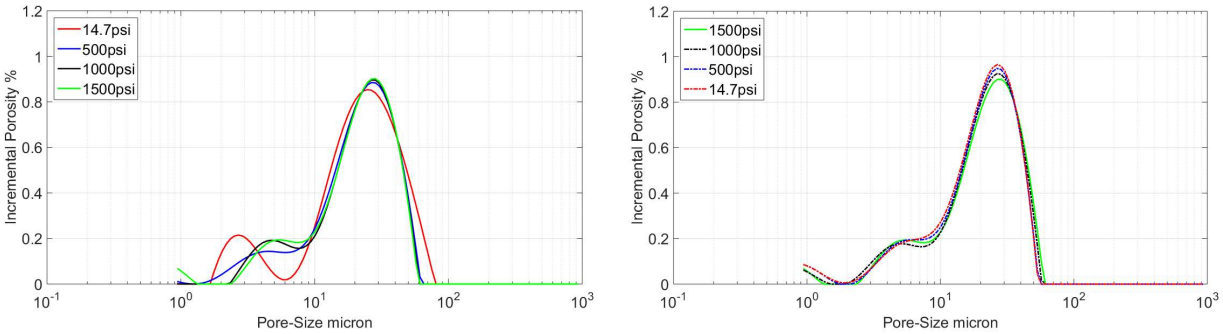

(a) (b)

Figure 4.2: NMR high pressure pore-size distribution for H1 sample. Data below 10 milliseconds is negligible due to the ringing effect caused by the limitation of the device. (a) Loading confining pressure. (b) Unloading confining pressure.

and NMR under 10 MPa confining pressure is shown on Figure 4.5. From the figure, very good correlation between the pore size of these two measurements can be seen.

The pore size distribution determined from NMR values and from the SIP data have lower values compared to the pore size calculated from the μ-CT images (Figure 3.2). The maximum pore size depicted from NMR for Berea sample is around 80 micrometers. However, pore size distribution acquired from μ-CT image for one slice of Berea sample shows maximum pore size distribution of around 165.8 micrometers. The larger pore size depicted from the μ-CT image compared to the NMR pore size distribution is due to CT image accepts all connected pores as one pore. The NMR pore size distribution is determined by accepting the pores as spherical voids which was explained in the methodology section. The lower value of pore size from the NMR is due to NMR relaxation is related to the interaction of water molecules with the pore wall, and

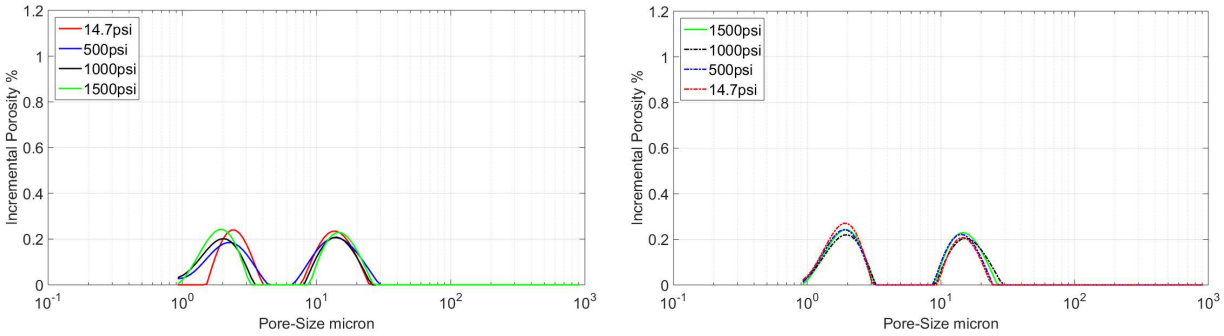

Figure 4.3: NMR high pressure pore-size distribution for J1 sample. Data below 10 milliseconds is negligible due to the ringing effect caused by the limitation of the device. (a) Loading confining pressure. (b) Unloading confining pressure.

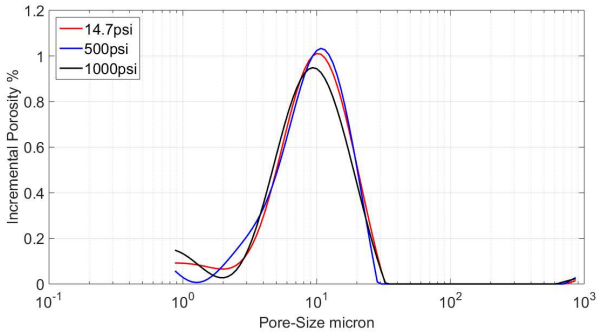

Figure 4.4: NMR high pressure pore-size distribution for 23A sample. Figure depicts the loading up to 7 MPa. Data below 10 milliseconds is negligible due to the ringing effect caused by the limitation of the device. The experiment could not be continued due to failure at 10 MPa.

their distance from the pore wall. Therefore, in one pore structure NMR can depict several pores.

4.2 Pore compressibility

Static pore compressibility for Berea, H1, J1, and 23A data was calculated from NMR pore size distribution and CMS-300 (helium porosimetry) data. Also, static pore compressibility was calculated for Berea sample using the pore size distribution determined from low frequency complex conductivity (SIP) to confirm the accuracy of the NMR and CMS-300 pore compressibility values. The dynamic pore compressibility was calculated from ultrasonic velocity measurements using Zimmerman's equation (Equation 2.1). The velocity measurements were run on Berea sample up to maximum pressure of 17 MPa, with 3.5 MPa increments. The experiment was conducted using PLP jacket, as mentioned on previous chapters. The ultrasonic velocities for H1, J1, and 23A data were acquired from provided data (Courtesy of Dr. Manika Prasad). The velocity measurements for these were not run on PLP jacket, due to the jacket diameter limitation of 1.5

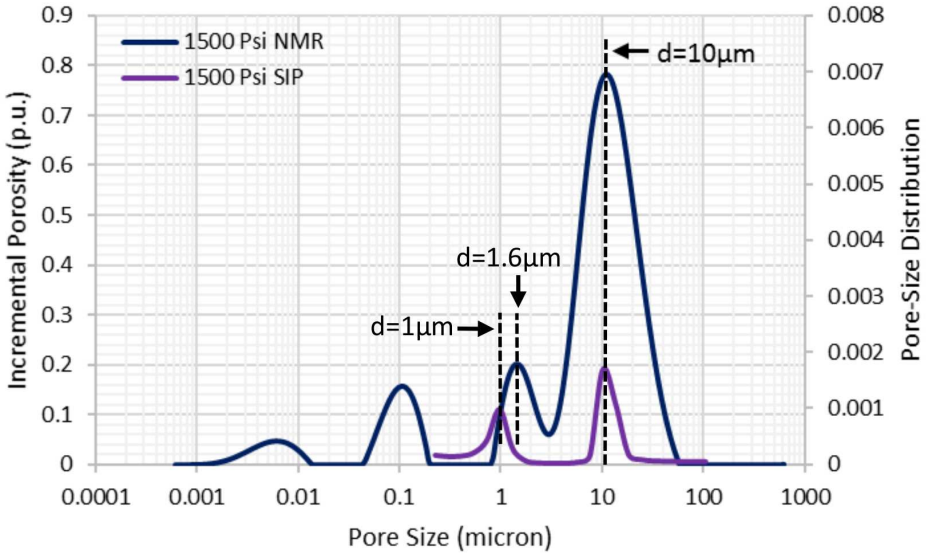

Figure 4.5: Pore size distribution comparison from NMR and SIP measurement under 10 MPa confining pressure for Berea sample. The figure shows good correlation between the pore size of these two measurements. This confirms the surface relaxivity value used to convert the NMR data from time domain to size domain.

inch. The H1, J1, and 23A cores used in this study were 1 inch in diameter. The ultrasonic velocities were also acquired from simultaneous NMR and acoustic measurement. However, I do not use this data due to bad signal acquisition caused by issues with grounding.

Table 4.1: Elastic moduli of the minerals, found in mineralogical composition of the studied samples. The elastic moduli values were taken from Avseth et al. (2010).

Mineral	Bulk Modulus (GPa)	Shear Modulus (GPa)
Quartz	37	44
Calcite	76.8	32
Dolomite	94.9	45
K-Feldspar	37.5	15
Ankerite	56.1	29.1
Plagioclase	75.6	25.6
Pyrite	147.4	132.5
Mixed Clays	2	1.4

Figure 4.6 shows the static pore compressibility determined by (Fatt 1958) and the pore compressibility calculated by me for Hibernia oil field samples. Comparison of the literature and pore compressibility

determined by me shows good correlation. Static pore compressibility measurement for Berea, H1, J1, and 23A samples are depicted in the Figure 4.7 to Figure 4.10. Figure 4.7 represents the static pore compressibility measurements for Berea samples using NMR, CMS-300, and SIP measurements. From the Figure 4.7, good correlation between the NMR, CMS-300 and SIP pore compressibility during pre-pressurization can be observed.

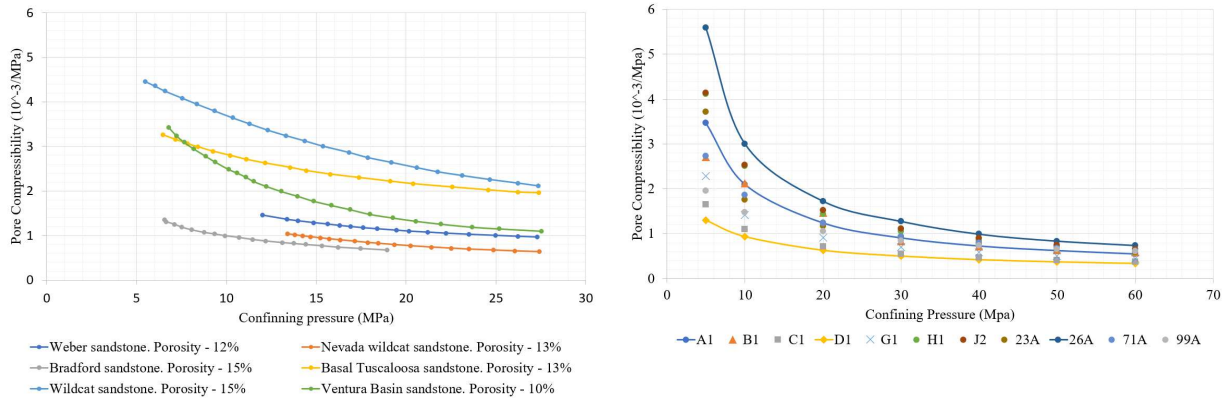

(a) (b)

Figure 4.6: Static pore compressibility. (a) Determined by Fatt for different sandstone formation with different porosity values (Fatt, 1958). (b) Pore compressibility for Hibernia oil field samples.

For H1, J1, 23A samples static pore compressibility were measured from the NMR and CMS-300 measurements. The SIP measurements were not run on these samples due to the limitation of the PLP jacket, as mentioned above. Figure 4.8 Figure 4.9, and Figure 4.10 represents the H1, J1, and 23A sample pore compressibility respectable. From these figures good correlation between NMR and CMS-300 pore compressibility can be observed. The correlation between the CMS-300 and NMR pore compressibility is depicted in Figure 4.11. From this figure good match between NMR and CMS-300 can be seen. The figure proves the viability of determining the pore compressibility using the NMR method.

From Figure 4.12, dynamic pore compressibility calculation for Berea sample in 0, 45, and 90 degrees can be seen. Also, the Figure presents the dynamic pore compressibility acquired from work conducted by Zimmerman (1991). Comparison of dynamic pore compressibility acquired from Zimmerman and calculated measurement show similar trend. However, the Zimmerman's pore compressibility displays higher values (80% greater) compared to the calculated data. This difference could be related to the disparity in porosity and mineralogy of the Berea sample used. From the micromechanical perspective, pore compressibility of the rocks is directly linked with the strength of the rock matrix, rock elastic properties, and the shape of the pores. By considering these aspects the rocks with weaker matrix will be expected to have larger pore

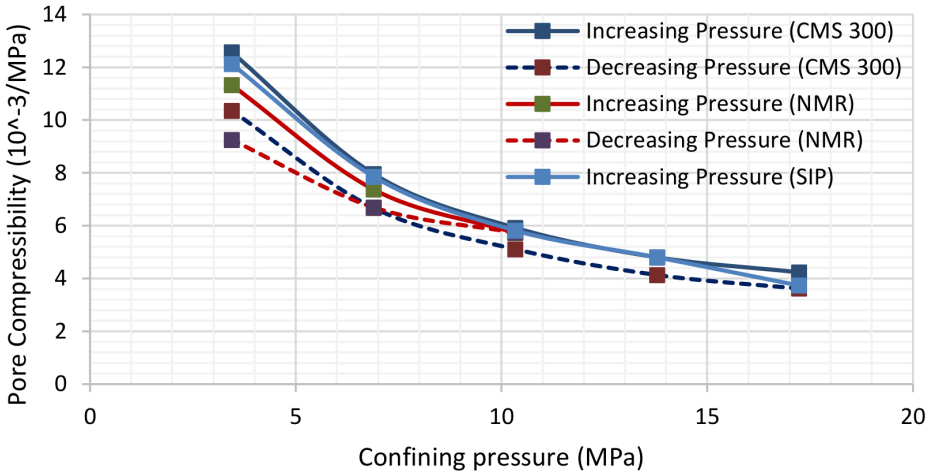

Figure 4.7: Total pore compressibility calculated for Berea sample (porosity - 23.1 %) using NMR, CMS-300, and SIP data points. The SIP pore compressibility was used to validate the NMR and CMS-300 pore compressibility. The aspect ratio determined for Berea sample from is $\alpha = 0.327$.

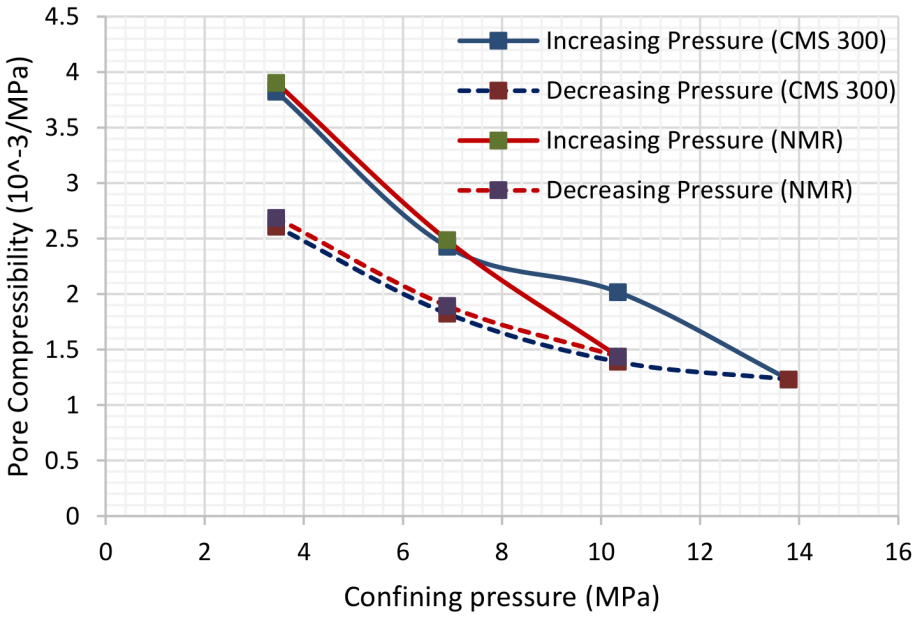

Figure 4.8: Pore compressibility calculated from NMR and CMS-300 data for H1 sample (porosity - 20 %). Good correlation between the two measurements can be observed. The lower compressibility of pores is due to the sample consist of large pore structures, additionally, mineralogy of the sample consists of 99% quartz. The aspect ratio determined for H1 sample is $\alpha = 0.464$.

compressibility compared with rocks composed of stiffer and stronger matrix.

The rock sample under great effective stresses, the complaint pores and cracks have tendency to close, which can result in significant stiffness of the sample. The pore compressibility, calculated during the hydrostatic loading test exhibit a sharp decrease during the initial microcrack closure stage, and finally reaching

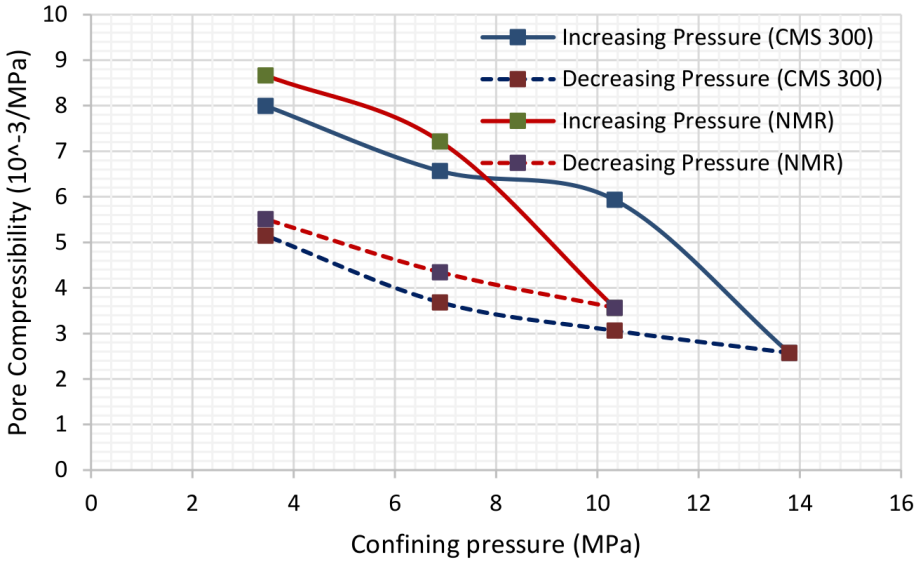

Figure 4.9: Pore compressibility calculated from NMR and CMS-300 data for J1 sample (porosity - 10.4 %) . Good correlation can be observed. High pore compressibility from this measurement can be related to sample composed of smaller pores, clay content of 3% determined from XRD. Also, the aspect ratio of pores, around $\alpha = 0.547$.

an asymptotic value at higher pressure which corresponds with the stiffness of the pores (Walsh 1965). This can be clearly seen from the dynamic measurement (Figure 4.13), however, as the static measurement were conducted up to maximum pressure of 10 MPa, the asymptotic value at higher pressure can't be observed.

As seen in Figure 4.7 to Figure 4.10, and Figure 4.13, the Berea, J1, and 23A samples have the greatest pore compressibility values. However, H1 sample exhibits lower pore compressibility value. Considering the Table 3.2 and Table 3.3, it can be observed that the porosity, and permeability does not correspond with the change in pore compressibility of the samples, as seen for H1 sample, which has high porosity (20%) and permeability (3.68 Darcy) values. This can also seen in Figure 4.6, where samples with similar porosity have different pore compressibilities. According to Hagin and Zoback (2004a), the intrinsic mineral frame anelasticity might be caused by the ductile minerals in the sample, such as clay which tend to have lower bulk and shear modulus (Table 4.1). As can be seen from the static and the dynamic pore compressibility measurements, the Berea, J1, and 23A samples have clay content of 2.53%, 3%, and 7%, respectively. While, H1 sample consist of purely (99%) quarts mineral, with no clay content. The increase in the clay content can increase pore compressibility of the rocks. Grain crushing and microfracture propagation could be another explanation for mineral frame anelasticity (Hagin and Zoback 2004). Also, the grain size, the cementation (Fatt 1958), and the aspect ratio of the pore structures can have great effect on the pore compressibility. Pores with lower pore aspect ratio will tend to have greater compressibility.

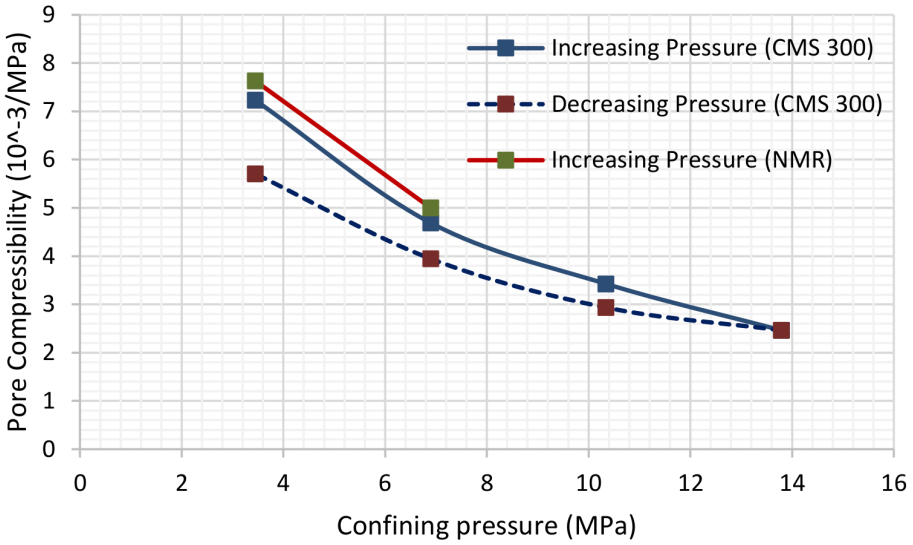

Figure 4.10: Pore compressibility calculated from NMR and CMS-300 data for 23A sample (porosity - 24.2 %). Similar good correlation can be viewed from the correlation determined from two measurement tools. Pore compressibility calculated from NMR pore size distribution was determined for only two pressure points. This was due to jacket rupture during the high-pressure NMR experiment. The compressibility determined for 23A sample has higher value. This is due to the higher clay content (7%) of the sample, determined from XRD. From XRD, the aspect ratio of around $\alpha = 0.852$ can be calculated, also, the sample consists of small pore structures.

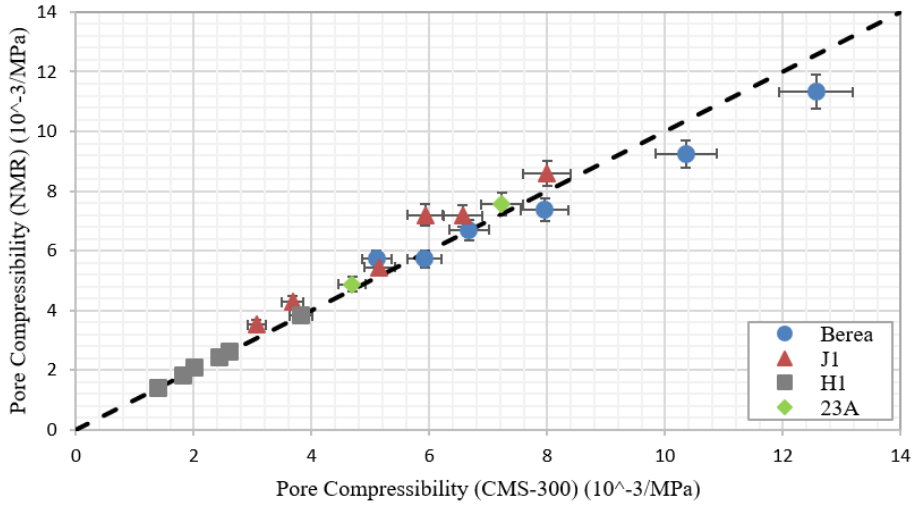

Figure 4.11: NMR and helium porosity (CMS-300) pore compressibility correlation. Good correlation between the two measurement can be observed.

From here we can conclude that the pore compressilbity is not affected by the porosity, but the pore volume change. The factors that can affect the change in pore volume are the mineral shear and bulk modulus, clay content, grain size, cementation, and the aspect ratio of the pores. The aspect ratio for Berea,

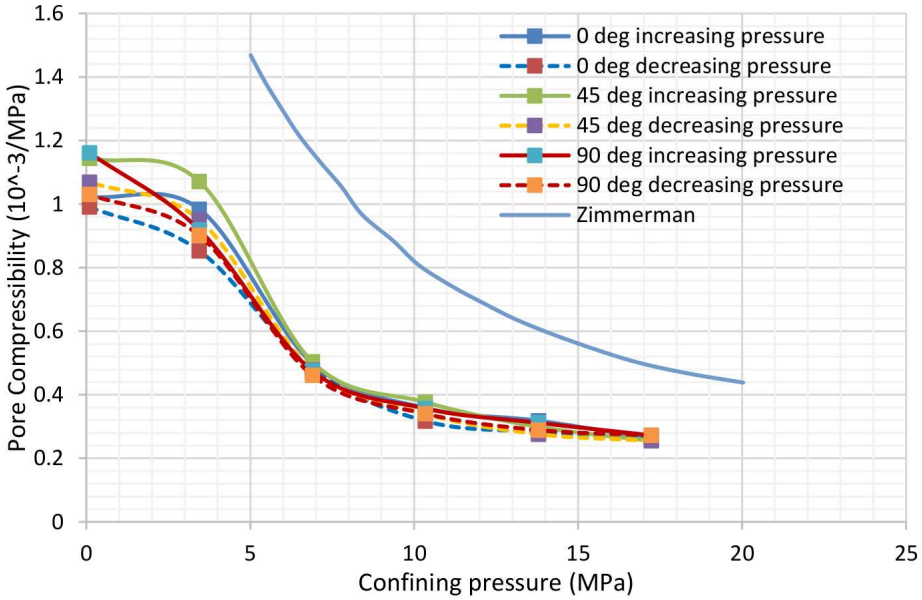

Figure 4.12: Dynamic pore compressibility for Berea sample determined for 0, 45, and 90 degrees, also the dynamic pore compressibility acquired from (Zimmerman et al. 1986). The calculated and acquired dynamic pore compressibility have similar trend. However, Zimmerman pore compressibility has higher value (80%) compared to the calculated pore compressibility. This could be related with the mineralogical content of the sample.

J1, H1, and the 23A samples are 0.327, 0.464, 0.547, and 0.852, respectively. These values were estimated from the CT image slices.

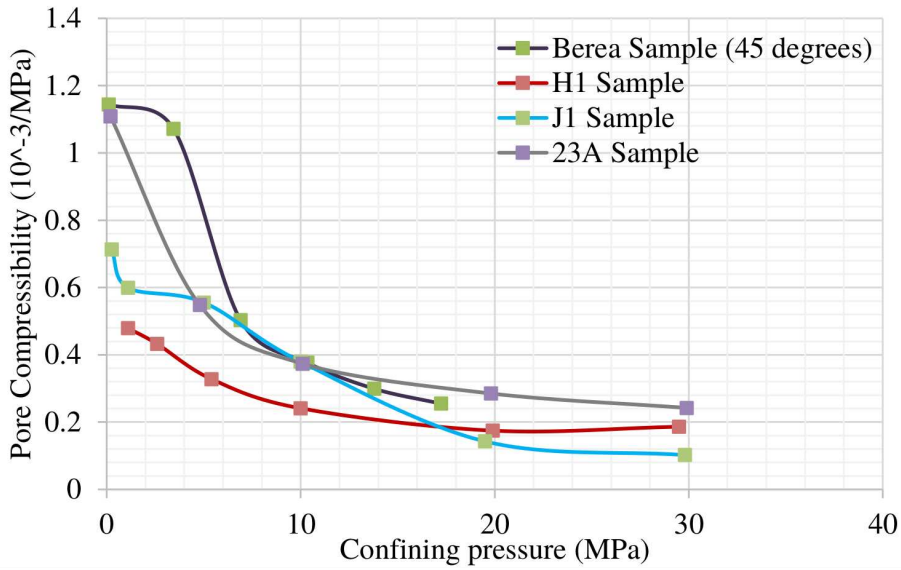

Figure 4.13: Dynamic pore compressibility for Berea, H1, J1, and 23A samples.

4.3 Pore cluster compressibility

Pore cluster compressibility was determined from the NMR pore size distribution for individual pore sizes. In this case, the pore size distribution was determined for Berea sample between 0.8 – 3 microns, and pore size larger than 3 microns. For H1 sample the pores size distribution was divided between 1 – 8 microns and pores larger than 8 microns, and for J1 samples pores were divided between 1 – 3 microns and pores larger than 3 microns. The 23A sample consists of bimodal distribution with pores larger than 1 micron. Figure 4.14, presents the pore compressibility determined for individual pore clusters. The pores between 0.8 – 3 microns for Berea, 1 – 8 microns for H1 sample, and 1 – 3 microns for J1 sample will be known as small pores. The pores larger than 3 microns for Berea, 8 microns for H1 sample, 3 microns for J1 sample, and 1 micron for 23A sample will be addressed as large pores. Figure 4.14(a) and Figure 4.14(b) represents the pore compressibility of small and large pores for Berea, H1, and 23A samples. From this figures expected decrease of large pores by increasing confining pressure can be observed. However, for smaller pores the compressibility values are in negative axis, this corresponds with the increase in number of pores in smaller pore size due to the compression of larger pores during the increasing confining pressure.

The J1 sample shows opposite effect as I mentioned before, this effect can be observed in Figure 4.14(c) and Figure 4.14(d). During the increasing confining pressure the small pores of J1 sample show compression, which is related with expected decrease in pore compressibility of these pores. However, larger pores show increase in number of pores or expansion of these pores. This could be due to pore crushing resulting in larger pore structures.

During the pore compressibility what we expect is decrease in all pores by increasing pressure. However, what we observe is negative pore compressibility values due to increase in number of pores. To understand this better more research must be conducted to determine the shifting pores and eliminate them.

4.4 Static-to-dynamic pore compressibility correlation

Figure 4.15 shows the correlation between the dynamic pore compressibility calculated from ultrasonic wave velocity and static pore compressibility obtained from helium porosity provided by Dr. Manika Prasad. The pore compressibility determined from NMR was not used to create the dynamic and static pore compressibility correlation. This is because, the pore compressibility determined from NMR and helium porosity had very good correlation.

The difference between the static and the dynamic pore compressibility can be due to cracks, presence of fractures, cavities, and planes of weakness and foliation (Oliveira et al. 2014). In general, higher number of discontinuities in rock, the higher discrepancy between static and dynamic pore compressibility. From the

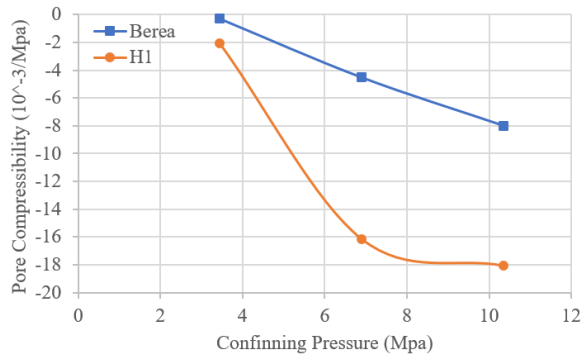

(a) Berea pore sizes 0.8 – 3 μm, H1 pore sizes 1 – 8 μm.

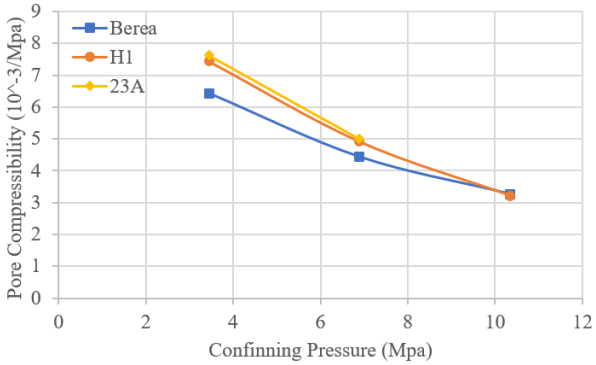

(b) Berea pore sizes > 3 μm, H1 pore sizes > 10 μm, and 23A pore size > 1 μm.

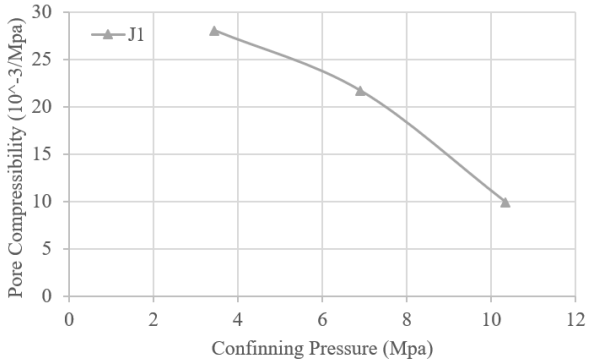

(c) J1 pore sizes 1 – 3 μm.

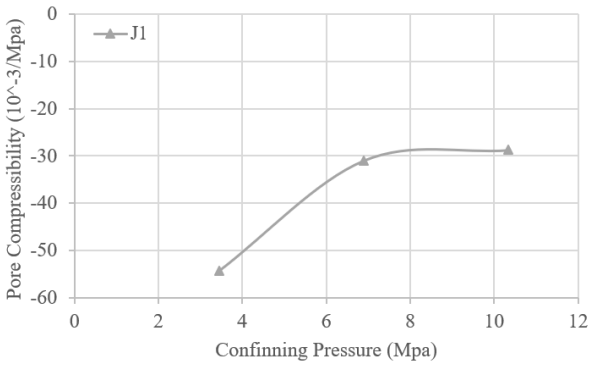

(d) J1 pore sizes > 3 μm.

Figure 4.14: Pore compressibility determined for individual pore clusters (loading cycle).

static and dynamic pore compressibility for Hibernia samples close relationship can be seen. The static pore compressibility is around 3 – 17 times larger than the dynamic pore compressibility at the initial pressure of 5 MPa, however, decrease in the difference between the static and dynamic pore compressibility can be seen by the increasing pressure. At 60 MPa the static pore compressibility is around 2 – 5 times larger than the dynamic measurement. This decrease in the difference can be related with the closer of crack and fractures in the samples by the increase in confining pressure.

Figure 4.16 shows the static and dynamic pore compressibility correlation determined by (Ceia et al. 2015) for carbonate samples. From this figure it can be observed that AC-001 and DP-001 samples have similar pore compressibility change as my samples. From this we can also determine that static and dynamic pore compressibility correlation should be determined for each reservoir, as the correlation determined by me for Hibernia oil field might not be applicable for other fields.

From this research we can conclude that pore compressibility determined from NMR is applicable, as it can be observed that the NMR pore compressibility and CMS-300 pore compressibility have a good

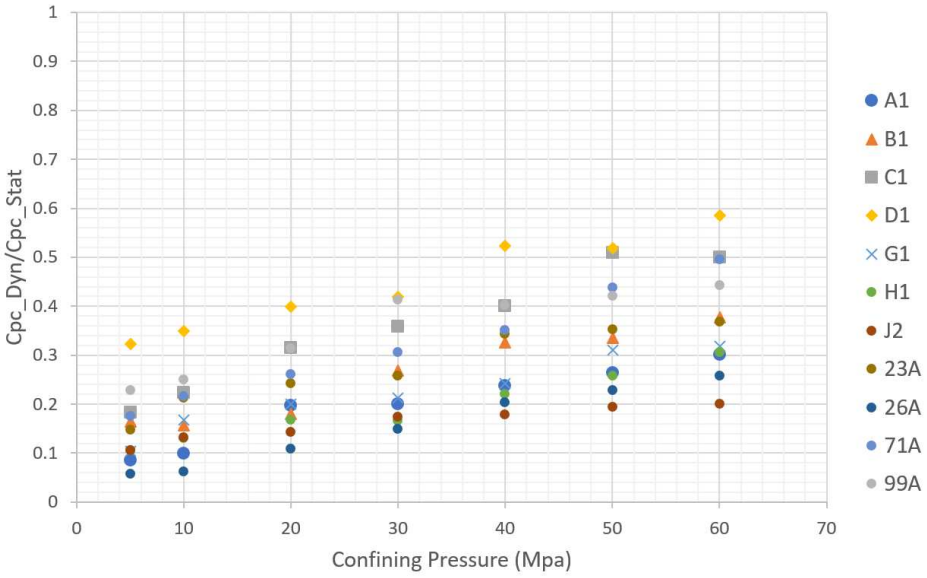

Figure 4.15: Static and dynamic correlation for Hibernia oil field samples. Static pore size distribution from NMR and dynamic pore size distribution from ultrasonic measurement.

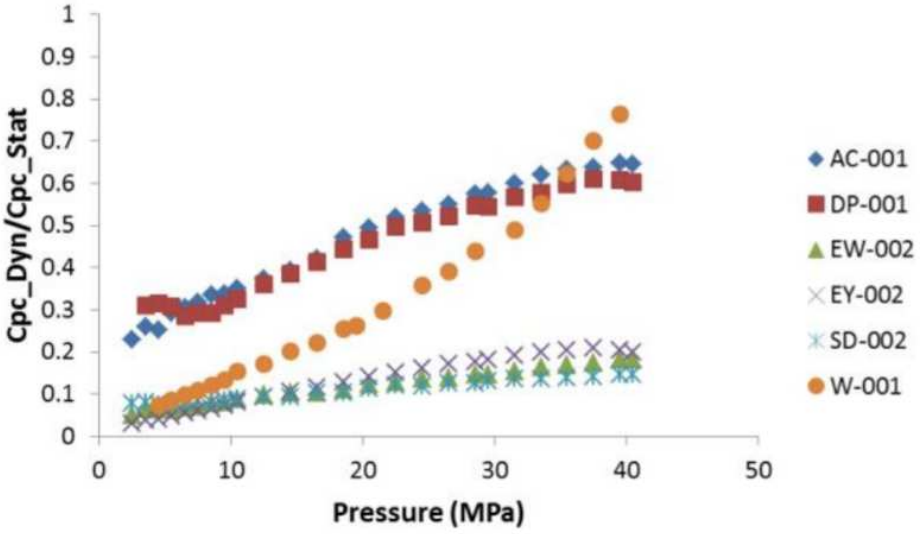

Figure 4.16: Static and dynamic pore compressibility correlation for carbonate samples (Ceia et al. 2015).

correlation. NMR pore compressibility can allow us to determine not only the total pore compressibility, but also the compressibility of individual pore clusters by distinguishing the pore cluster sizes. However, further research on this must be conducted to eliminate the pore shift caused by increase in number of smaller pores during the increasing confining pressure. Also, the increase in the percentage of metal elements in the sample can affect the NMR data acquisition, by decreasing the signal to noise ratio. However, this problem was not found in my study, due to the samples having little or no pyrite minerals. The static and

the dynamic pore compressibility determined from this research show that the compressibility of the pores are not correlated by porosity value, but to the pore volume change. The higher porosity will not result in higher pore compressibility. The pore volume change can be related to the mineral shear and bulk modulus, clay content, grain size, cementation, and the aspect ratio of the pores. Static pore compressibility of 2 –5 times larger than the dynamic pore compressibility can be observed, similar correlation between static and dynamic pore compressibility can be seen in the literature.

The NMR pore compressibility acquired from my research can be used in geomechanical models to predict reservoir compaction and subsidence. Also, the pore compressibility determined for each pore cluster can determine which pores will have the greatest effect on the reservoir compaction. This data can also be used to differentiate fracture and pore change during the production life of the reservoir.

CHAPTER 5
CONCLUSIONS AND FUTURE WORK

SIP and CMS-300 pore compressibility data was used to determine the accuracy of the pore compressibility determined from the NMR pore size distribution. Good correlation between NMR, SIP, and CMS-300 pore compressibility can be observed.

From the determined pore compressibility for four samples, Berea, J1, H1, and 23A respectively show that pore compressibility is not only affected by the sample porosity and permeability, but also the mineral bulk and shear modulus, and the clay content, which acts as grain cement. Also, the aspect ratio of the pores plays a major role for the pore compressibility. The samples that have smaller aspect ratio have higher pore compaction. A decrease in pore size and an increase in the number of smaller pores was observed. This can be caused by the closure of fractures, collapse of smaller pores, and the compression of larger pores. This research proves that using the NMR we can not only determine the total pore compressibility, but also the compressibility of individual pore clusters. The pore compressibility determined from NMR can be used to model reservoir compaction and subsidence. Also, the individual pore cluster compressibility determined from NMR can be used to determine which pores will more contribute to these issues.

The static and dynamic pore compressibility show good correlation. From the static and dynamic pore compressibility comparison, higher values for static measurement compared to dynamic measurement can be observed. This correlation is usable to convert the dynamic acquired data into static data, especially for this formation. This acquired correlation can be used in geomechanical modeling of the reservoir behavior.

5.1 Future work

Based on the pore compressibility study, I recommend to address these following issues in the future

- The following experiment discussed in this study can be conducted under higher confining pressures to observe the reservoir behavior. The experiments for this research were conducted under constant pore pressure and changing confining pressure. To recreate reservoir condition it would better to change the pore pressure and keep the confining pressure constant.

- The aspect ratios determined from the μ-CT can be used in Differential Effective Medium modeling to validate laboratory data. Due to the limitation of the device, the aspect ratio determined in this research was for pores larger than 2.25 micron. Scanning electron microscopy (SEM) images can be acquired for this samples to determine the aspect ratio of smaller pores.

- Performing μ-CT imaging under elevated confining pressure would allow to gain a deeper insight into the change of the rock matrix and pore structure.
- Using the Differential Effective Medium modeling we can model the increase and decrease in cluster of different sized pores and isolate the clay effect.

REFERENCES CITED

API RP 40, Recommended Practices for Core Analysis. 1998. Washington, DC: API.

Avseth, P., Mukerji, T., and Mavko, G. 2010. *Quantitative seismic interpretation: Applying rock physics tools to reduce interpretation risk*. Cambridge: Cambridge university press.

Brown, D.M., McAlpine, K.D., and Yole, R.W. 1989. Sedimentology and sandstone diagenesis of Hibernia Formation in Hibernia oil field, Grand Banks of Newfoundland. *AAPG Bulletin*, **73**(5), 557–575.

Carpenter, C.B., and Spencer, G.B. 1940. *Measurements of compressibility of consolidated oil-bearing sandstones*. Vol. 3540. Washington, D.C.: United States Department of the Interior, Bureau of Mines.

Ceia, M., Misságia, R., Neto, I. L., et al. 2015. Comparison of static and dynamic pore compressibilities in carbonate rocks. 14th International Congress of the Brazilian Geophysical Society & EXPOGEF, Rio de Janeiro, Brazil, 3-6 August.

Coates, G.R., Xiao, L., and Prammer, M.G. 1999. *NMR logging: principles and applications*. Houston, Texas: Haliburton Energy Services.

Dunn, K.J., Bergman, D.J., and Latorraca, G.A. 2002. *Nuclear magnetic resonance: Petrophysical and logging applications*. Vol. 32. Oxford: Elsevier Science.

Fatt, I. 1958. Compressibility of sandstones at low to moderate pressures. *AAPG Bulletin*, **42**(8), 1924–1957.

Geertsma, J. 1957. The effect of fluid pressure decline on volumetric changes of porous rocks. *Petroleum Trans: AIME*, **76**(3), 6414–6419. SPE–728–G.

Hagin, P.N., and Zoback, M.D. 2004. Viscous deformation of unconsolidated reservoir sands – Part 2: Linear viscoelastic models. *Geophysics*, **69**(3), 742–751.

Hall, H.N. 1953. Compressibility of reservoir rocks. *Journal of Petroleum Technology*, **5**(01), 17–19. SPE–953309–G.

Hasanov, A.K. 2014. *Reservoir transport and poroelastic properties from oscillating pore pressure experiments*. MS thesis, Colorado School of Mines, Golden, CO.

Hounsfield, G.N. 1980. Computed medical imaging. *Medical physics*, **7**(4), 283–290.

Jones, S.C. 1972. A rapid accurate unsteady-state Klinkenberg permeameter. *Society of Petroleum Engineers Journal*, **12**(05), 383–397. SPE–3535–PA.

Kuila, U. 2013. *Measurement and interpretation of porosity and pore-size distribution in mudrocks: The hole story of shales*. Ph.D. thesis, Colorado School of Mines, Golden, CO.

Kuila, U., McCarty, D.K., Derkowski, A., et al. 2014. Total porosity measurement in gas shales by the water immersion porosimetry (WIP) method. *Fuel*, **117**, 1115–1129.

Li, C., Chen X., and Du, Z. 2004. A new relationship of rock compressibility with porosity. Presented at the SPE Asia Pacific Oil and Gas Conference and Exhibition, Perth, Australia, 18-20 October. SPE-88464.

Li, S., Tang, D., Pan, Z., et al. 2013. Characterization of the stress sensitivity of pores for different rank coals by nuclear magnetic resonance. *Fuel*, **111**, 746–754.

Macini, P., and Mesini, E. 1998. Static and dynamic reservoir rock compressibility at high pressure. Presented at the Abu Dhabi International Petroleum Exhibition and Conference, Abu Dhabi, U.A.E., 11-14 October. SPE-49549.

Marchina, P., Brousse, A., Fontaine, J., et al. 2004. In-situ Measurement of Rock Compressibility in a Heavy Oil Reservoir. Presented at the SPE International Thermal Operations and Heavy Oil Symposium and Western Regional Meeting, Bakersfield, California, U.S.A., 16-18 March. SPE-86940.

Marschall, D., Gardner, J.S., Mardon, D., et al. 1995. Method for correlating NMR relaxometry and mercury injection data. Presented at the 1995 SCA Conference, Houston, Texas, U.S.A., 12 September. No-9511.

Oliveira, G., Ceia, M., Misságia, R., et al. 2014. Pore volume compressibilities derived from Helium porosimetry and elastic measurements. Presented at the 2014 SEG Annual Meeting, Denver, Colorado, U.S.A., 26-31 October.

Panfiloff, A. 2016. *Experimental evaluation of dynamic elastic properties and anisotropy in shales*. MS thesis, Colorado School of Mines, Golden, CO.

Poston, S.W., and Chen, H.Y. 1987. The simultaneous determination of formation compressibility and gas-in-place in abnormally pressured reservoirs. Presented at the SPE Production Operations Symposium, Oklahoma City, Oklahoma, U.S.A., 8-10 March. SPE-16227.

Revil, A., Florsch, N., and Camerlynck, C. 2014. Spectral induced polarization porosimetry. *Geophysical Journal International*, **198**(2), 1016–1033.

Saidian, M. 2015. *Effect of rock composition and texture on pore size distributions in shales: Applications in low field nuclear magnetic resonance*. Ph.D. thesis, Colorado School of Mines, Golden, CO.

Suman, A. 2009. *Uncertainties in Rock Pore Compressibility and Effects on Seismic History Matching*. Ph.D. thesis, Stanford University, Stanford, CA.

Walsh, J.B. 1965. The effect of cracks on the compressibility of rock. *Journal of Geophysical Research*, **70**(2), 381–389.

Yildiz, T. 1987. Prediction of in-situ formation compressibility from production data. Presented at the SPE/ISRM Rock Mechanics in Petroleum Engineering, Trondheim, Norway, 8–10 July. SPE-47379-MS.

Zimmerman, R. W., Somerton, W. H., and King, M. S. 1986. Compressibility of porous rocks. *Journal of Geophysical Research: Solid Earth*, **91**(B12), 12765–12777.